# Multi-Phase Fracture-Matrix Interactions Under Stress Changes

Seventh Semi-Annual Report

Reporting Period
September 21, 2004 – March 20, 2005

Principal Authors:
A.S. Grader, D. Elsworth, P.M. Halleck, F. Alvarado, A. Alajmi, Z. Karpyn,
N. Mohammed, S. Al-Enezi

Report Issue Date: June 15, 2005

DOE Award Number: DE-FC26-01BC15355

Submitting Organization:
The Pennsylvania State University
The Energy Institute
A.S. Grader
203 Hosler Building
University Park, PA 16802

## DISCLAIMER

**ABSTRACT**

The main objectives of this project are to quantify the changes in fracture porosity and multi-phase transport properties as a function of confining stress. These changes will be integrated into conceptual and numerical models that will improve our ability to predict and optimize fluid transport in fractured system. This report details our progress on: **a**. *developing the direct experimental measurements of fracture aperture and topology and fluid occupancy using high-resolution x-ray micro-tomography,* **b**. *qunatifying the effect of confining stress on the distribution of fracture aperture* , *and* **c**. *characterization of shear fractures and their impact on multi-phase flow*.

The three-dimensional surface that describes the large-scale structure of the fracture in the porous medium can be determined using x-ray micro-tomography with significant accuracy. Several fractures have been scanned and the fracture aperture maps have been extracted. The success of the mapping of fracture aperture was followed by measuring the occupancy of the fracture by two immiscible phases, water and decane, and water and kerosene.

The distribution of fracture aperture depends on the effective confining stress on the nature of the rock and the type and distribution of the asperities that keep the fracture open. Fracture apertures at different confining stresses were obtained by micro-tomography covering a range of about two thousand psig. Initial analysis of the data shows a significant aperture closure with increase in effective confining stress. Visual descriptions of the process are shown in the report while detailed analysis of the behavior of the distribution of fracture aperture is in progress. Both extensional and shear fractures are being considered.

The initial multi-phase flow tests were done in extensional fractures. Several rock samples with induced shear fracture are being studies, and some of the new results are presented in this report. These samples are being scanned in order to quantify the distribution of apertures and the nature of the asperities. Low resolution images of fluids in a sample with a shear fracture were performed and they provide the confidence that flow patterns and saturations could be determined in the future.

A series of water imbibition tests were conducted in which water was injected into a fracture and its migration into the matrix was monitored with CT and DR x-ray techniques. The objective is to understand the impact of the fracture, its topology and occupancy on the nature of mass transfer between the matrix and the fracture. Counter-current imbibition next to the fracture was observed and quantified, including the influence of formation layering.

## TABLE OF CONTENTS

**LIST OF FIGURES**

**LIST OF TABLES**

## INTRODUCTION

Natural and artificially-induced fractures in a reservoir have a great impact on fluid flow patterns and on the ability to recover hydrocarbons. In tight formations, the naturally fractured system provides access to the hydrocarbon fluids stored in the matrix. Fractures can have a negative effect on recovery processes when they form bypassing paths, especially in production-injection systems. For example, injected fluid may preferentially flow through the fractures leaving behind inaccessible and non-contacted hydrocarbons. Fractures can enhance the efficiency of displacement operations when the main direction of flow is perpendicular to the direction of the fractures. Fractures may also be non-conductive and form barriers to fluid flow. The mass transport between the fractures and the surrounding matrix has an important role in being able to predict and optimize the recovery processes from fractured reservoirs. As production occurs and pore pressures decline, the net confining stress on the rock increases. This project focuses on the effects that changes in confining stress have on the transport properties of the fracture-matrix system. The confining stress has an impact on the fracture aperture and therefore on multiphase fluid transport properties (*Barton et al.*, 1985, *Gentier et al.*, 1997). We propose to quantify the changes in fracture porosity and saturation distribution under steady and non-steady flow in both the fracture and the adjoining matrix. The quantitative changes will be obtained by low and high resolution X-ray computerized tomography (CT) imaging (*Vinegar and Wellington*, 1987), and then these changes will be used in an inverse simulation process to quantify changes in permeabilities and to suggest up-scaling procedures.

We propose a fracture-matrix interaction program with the following objectives:

• Quantify the effects of confining stress on fracture topology and aperture and porosity.

• Quantify the changes in two-phase fracture permeabilities as a function of stress.

• Determine the effect of stress on oil-water transport between the fracture and the matrix.

• Determine the effects of stress on recovery processes in the presence of fractures.

• Use inverse simulation of four-dimensional saturation data for up-scaling.

We approach multi-phase flow in stressed fractured rocks experimentally and computationally. We will use multi-phase injection into confined rock samples that contain natural fractures or artificially induced ones. We will quantify the saturation distribution temporally and spatially (four-dimensional) using our new imaging facility and The Center for Quantitative Imaging. We will also monitor the pressure behavior of the sample and confining fluids. The resulting four-dimensional distribution of saturations and pressure histories will form the basis for multi-phase fluid flow simulation with the ultimate goal of quantifying the changes in the fluid flow characteristics of the rock as a function of the net confining stress. This combined experimental/computational approach will lead to advances in our understanding of the effects in-situ stress on recovery processes.

## EXECUTIVE SUMMARY

The main objectives of this project are to quantify the changes in fracture porosity and multi-phase transport properties as a function of confining stress. These changes will be integrated into conceptual and numerical models that will improve our ability to predict and optimize fluid transport in fractured system. The project has five tasks:
1. Quantify the effects of confining stress on fracture topology and aperture and porosity.
2. Quantify the changes in two-phase fracture permeabilities as a function of stress.
3. Determine effects of stress on oil-water transport between the fracture and the matrix.
4. Determine the effects of stress on recovery processes in the presence of fractures.
5. Use inverse simulation of four-dimensional saturation data for up-scaling.
This report focuses mainly on tasks 1, 2 and 5.

**Fracture Topology, Aperture, and Fluids:** A new multi-phase experiment was conducted during the current reporting period. The experiment included the mapping of the distribution of fracture apertures and the distribution of two fluid phases in the fracture. There is a clear relationship between the presence of the non-wetting phase and the large fracture apertures, as expected from capillary stability considerations. The experiments included imaging while flowing and during segregation. The experiment was done at low confining stress using the newly designed and manufactured core holder. Significant effort has been devoted to managing and mining the three-dimensional digital data describing the experiment that included eight temporal sequences of more than three thousand micro-tomography slices per sequence.

**Fracture Closure Under Confining Stress:** The experiment documented in this report explored the ability of micro-tomography to quantify the changes in the distribution of fracture apertures with different confining stresses. The experiment was performed under dry conditions with an extensional fracture, and a confining pressure range between 100 and 2500 psig. The closure of the fracture is documented and we are in the process of quantifying the increase in the contact area, the decrease in fracture volume, and change in the distribution of fracture apertures.

**Shear Fracture:** Shear fractures have different properties than extensional fractures. We have artificially fractured several samples in shear mode and are currently studying the single- and two-phase fluid flow in these samples using external measurements of fluid volumes, pressure gradients, and internal saturation and structure measurements using micro-tomography. The absolute permeability of three samples was reduced by about 30% after the fracturing process. One sample (so far) was scanned to reveal a very complicated fracture and sub-fractures along the curved fracture surface. There are large asperities that are very different in structure than the asperities created in an extensional fracture.

**Modeling of Fracture-Matrix Fluid Flow Interactions:** Some previously performed two-phase flow experiments are being analyzed. In one of these experiments, a layered sample was fractured at the inlet end, with an axial fracture that extended only to the

middle of the sample, creating a fracture tip. The oil loading process is being modeled. Two dimensional simulations are being integrated into a full three-dimensional model. Properties from the two-dimensional systems are used as the starting point for the three-dimensional simulations. Early results indicate that there is cross flow between the layers during the oil loading period.

## EXPERIMENTAL METHOD AND PROCEDURES

The experimental system used in this project includes a multi-phase fluid flow system, a core holder assembly that can provide controlled confining pressure, and an x-ray computed tomography system. A schematic of the system is shown in Figure 1 and photographs of the medical and the industrial scanners are shown in our first quarterly report. Most of the details of the fluid flow system can be found in *Alajmi and Grader* (2000). Two new core holders were acquired. These are tri-axial cells with high pressure ratings and elevated temperatures. The rock samples may have a diameter of up to 25 mm and a length of up to 300 mm. These core holders will be used to study the effects of confining stress and fracture aperture on two phase flow. A new core holder was designed and built for low confining pressure. This core holder is made of polycarbonate and is clear. The advantage of this low pressure core holder is that it has a low x-ray attenuation allowing efficient micro-tomography operations.

The Computed Tomography (CT) system consists of an ionized x-ray source, a detector, a translation system, and a computer system that controls motions and data acquisition. The x-ray source has a Tungsten target with a focal spot of 5 microns. It produces a cone beam that passes through the core and activates the detector. The image intensifier detector surface releases electrons that are then focused on a screen that is photographed by a high-resolution (1024x1024) camera with a frequency of 15 Hz. The sample is

rotated 360 degrees in the x-ray beam while the detector is providing attenuation views to the data acquisition computer. After the sample is rotated a complete turn, the system reconstructs a slice, a cross-sectional image of the attenuation values that represents a combination of the density and the apparent atomic number of the sample and the imaged position. The imager operates in volume mode where several separate slices are collected in one rotation. In the example shown in the report, up to 41 slices were acquired in a single rotation. After each rotation, the sample is translated axially to a new scanning position, thus, allowing a continuous three-dimensional coverage of the sample.

## RESULTS AND DISCUSSION

### MATRIX-FRACTURE INTERACTION – MODELING COUNTER-CURRENT IMBIBITION

This experiment focuses on mass transport between the fracture and the matrix under imbibition conditions. The entire core was oil saturated and then a fixed amount of water was injected strictly into the fracture and then allowed to equilibrate. Counter-current imbibition created water flow from the fracture to the matrix and oil flow from the matrix to the fracture. This is an essential process to understand and quantify as it is the main displacement production mechanism that allows us to extract hydrocarbons from matrix blocks into the transmitting fractured network. In this section, conceptual modeling of water imbibing into the matrix from the fracture, and the counter-flow of oil into t he fracture are considered. The experimental system was described in the previous report, and is not presented here.

Reservoir simulation at laboratory scale was implemented to assist in understanding various experimental observations and flow mechanisms taking place during capillary imbibition in fractured media. The simulation packages used were developed by Computer Modeling Group, Inc. (CMG). The specific tools used were Builder for pre-processing applications, Results for post-processing applications, and IMEX: IMplicit-EXplicit Black Oil Simulator for the actual two-phase model. The input files created are presented in Appendix **B**.

The first case study consisted of a two-dimensional vertical reservoir with dimensions 12.5 mm x 48 mm, representing one half of the system. The sample radius was approximately 12.5 mm and its height 48 mm, which were selected as the reservoir dimensions. Figure 1 shows the grid used to represent fracture and matrix in this model. The grid has 13 blocks in the "i" direction (horizontal) and 48 blocks in the "j" direction (vertical). The blue column represents the fracture and the grid blocks in red are matrix blocks. The dimensions of each fracture blocks was 0.5 x 1 x 1 mm and the dimensions of each matrix block was 1 x 1 x 1 mm.

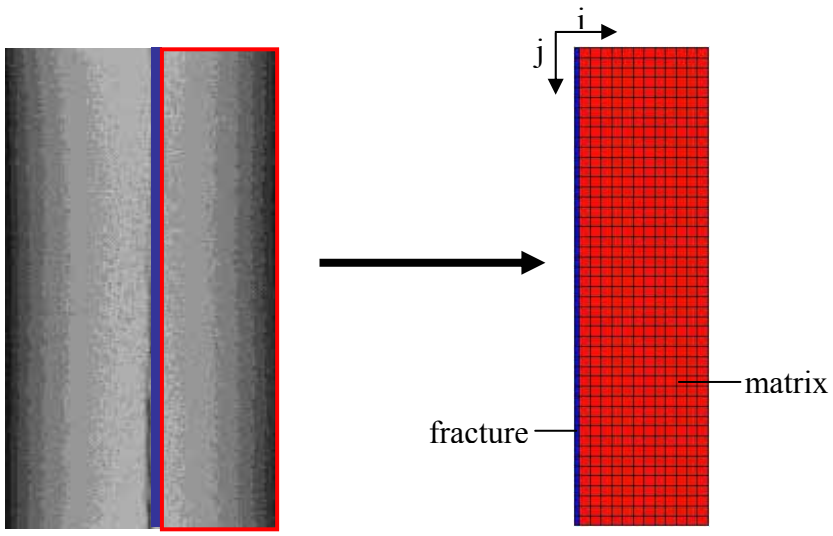


Figure 1: Grid model for two-dimensional imbibition.

Rock and fluid properties were estimated from those reported by Alajmi (2003), who conducted numerical history matching of two-phase flow experiments in fractured Berea samples, using similar fluids and rock. Alajmi (2003) used 64 md of absolute permeability in all directions and an average porosity of 17.5 % in his two-dimensional model. Same values were used in the current two-dimensional model. Fracture porosity was calculated from the ratio between the actual volume of the fracture, obtained from CT data, and the bulk volume of the simulated fracture, denoted in blue in Figure 1. A volume equivalent to the simulated two-dimensional grid was identified on the CT data and used to calculate the actual volume of the fracture. Table 1 presents a summary of porosity and permeability values used in the present two-dimensional model.

| Table 1: Rock properties assigned to fracture and matrix in two-dimensional model. | |
|---|---|
| PROPERTY | VALUE |
| Fracture permeability [md] | 5,000 (isotropic) |
| Matrix permeability [md] | 64 (isotropic) |
| Fracture porosity [fraction] | 0.38 |
| Matrix porosity [fraction] | 0.175 |
| | |

Capillary pressure and relative permeability curves used in the two-phase imbibition model are presented in Figures 2 and 3. The curves assigned to the matrix are similar to those presented by Alajmi (2003). Residual oil saturation in the fracture is larger than that in the matrix due to oil trapping in the fracture.

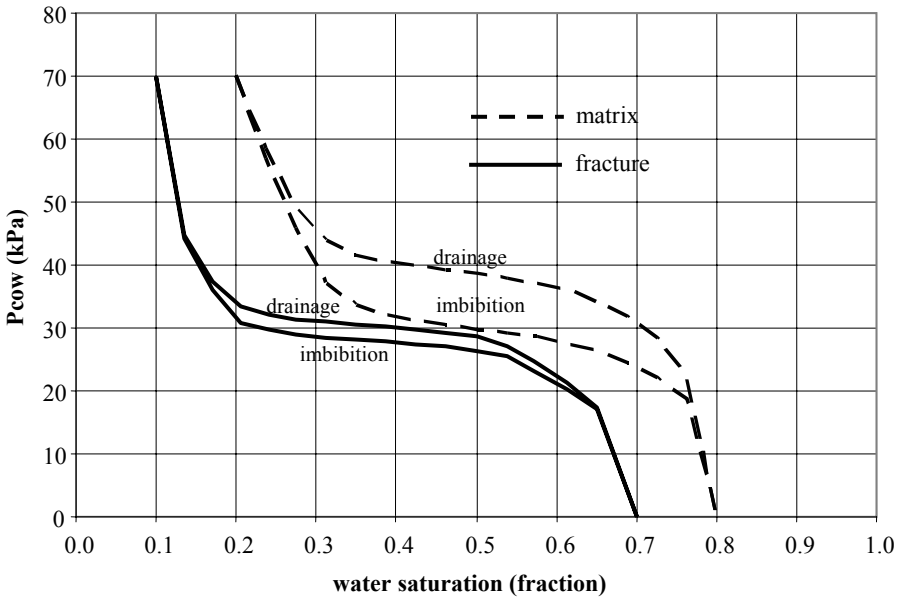


Figure 2: Capillary pressure curves used for two-dimensional model.

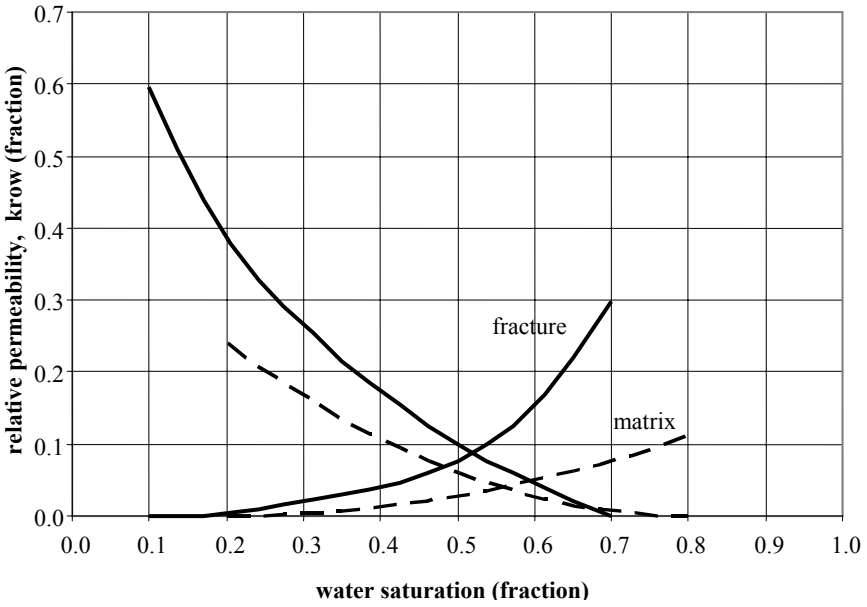


Figure 3: Relative permeability curves used for numerical modeling.

Initially, fracture capillary pressures were turned off in the two-dimensional model and only matrix capillary pressures were accounted for. As a result, simulated saturation maps were far from capturing the real imbibition process. Figure 4 shows the simulated maps using fracture capillary pressure equal to zero. The simulated water front is significantly shorter than the one in the digital radiographies. The imbibing front in the experimental maps was able to reach much farther than what the model could predict. The discrepancy between experiments and simulation suggests that an additional driving force is elevating the water through the fracture sample, just as capillarity would do.

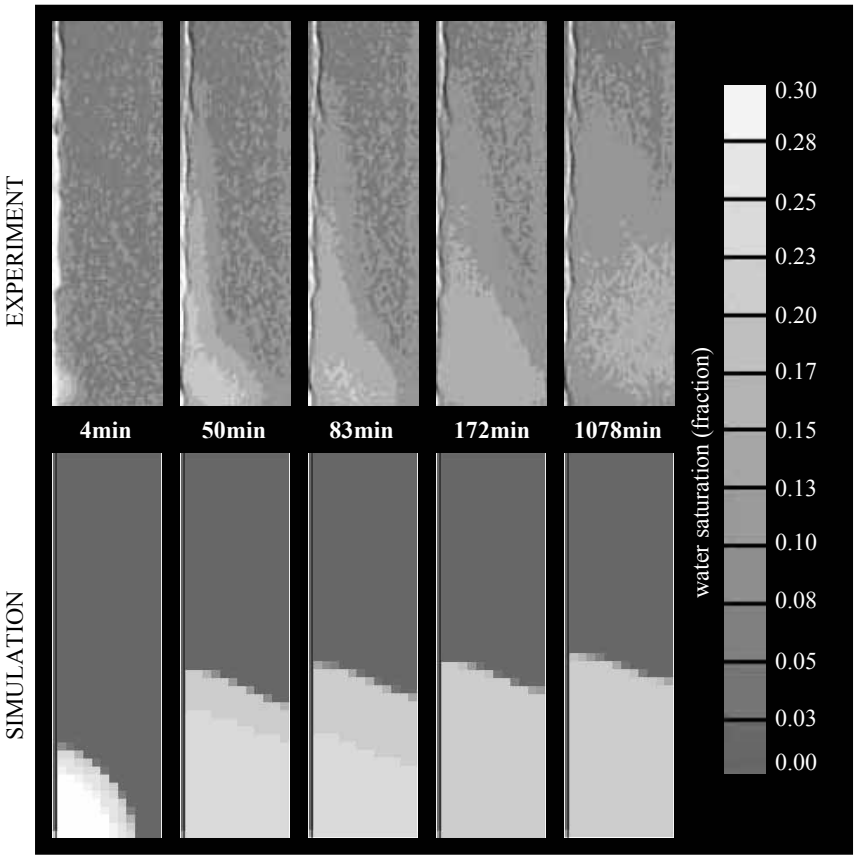


Figure 4: Simulated water front using fracture capillary pressure equal to zero.

A second case scenario was tested where both fracture and matrix had the same assigned capillary pressure curves. This simulated scenario delivered the saturation maps presented in Figure 5.

A comparison between simulated saturation maps in Figures 4 and 5 demonstrated strong sensitivity with respect to fracture capillary pressure. Fracture capillary pressure is often regarded as negligible in fractured reservoir simulations, but experimental observation has proven otherwise. Fracture capillary pressures are a major contributor to flow, and their impact must not be overlooked by the modeler. Accounting for capillary forces in the fracture is essential for successful modeling of fracture-matrix flow. Contact areas in the fracture provide passages under strong capillary action, which are able to drive

wetting fluids into the rock matrix. Such behavior can be captured by means of fracture capillary pressures and void structure. Water available to the fracture immediately reaches for the narrowest gaps and imbibes the rock matrix near contact areas. Fracture capillary forces are especially important when the rate of injection is close to or less than the matrix's capacity to transport fluids.

A third modification on the fracture capillary pressure curve led to the results presented in Figure 6. In this case, fracture capillary pressures assigned to the model were lower than those assigned to the matrix. For most part of the mobile saturation window, matrix capillary forces are higher than those in the fracture.

Capillary-driven flow in fractured media and the mechanism by which oil and water exchange places is governed by aperture distribution, capillarity, permeability and wettability. They compete to guide fluid flow between fracture and matrix, and through the different layers of the rock. One of the hypotheses posed in this work was that capillary-driven imbibition would take place mainly due to local counter-current flow of wetting and non-wetting phases. However, experimental observations suggest that counter-current flow prevails in the direction perpendicular to the fracture surface, while co-current flow dominates longitudinal imbibition, parallel to the fracture plane.

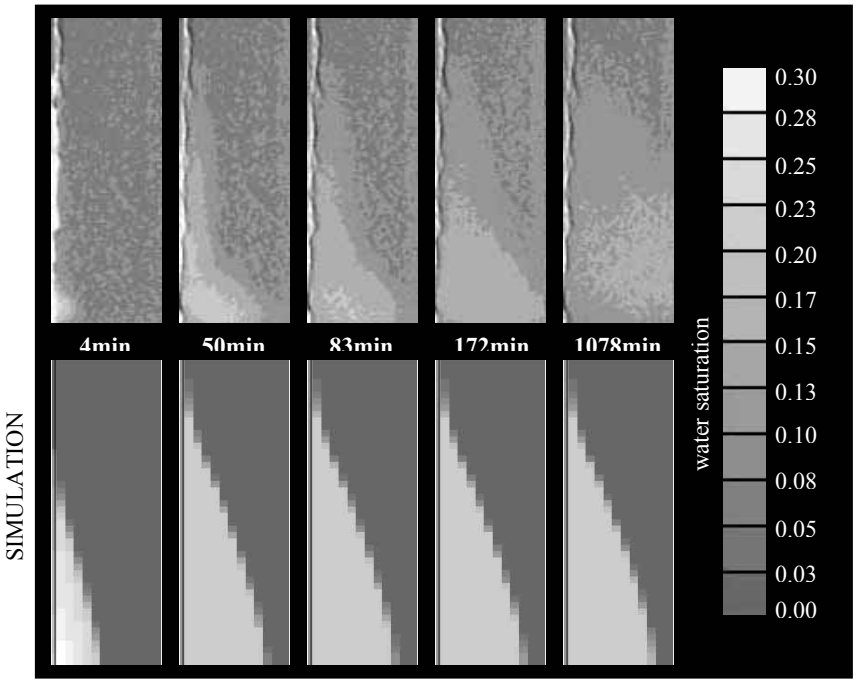


Figure 5: Simulated cumulative water front using similar capillary pressure curves in the fracture and the matrix.

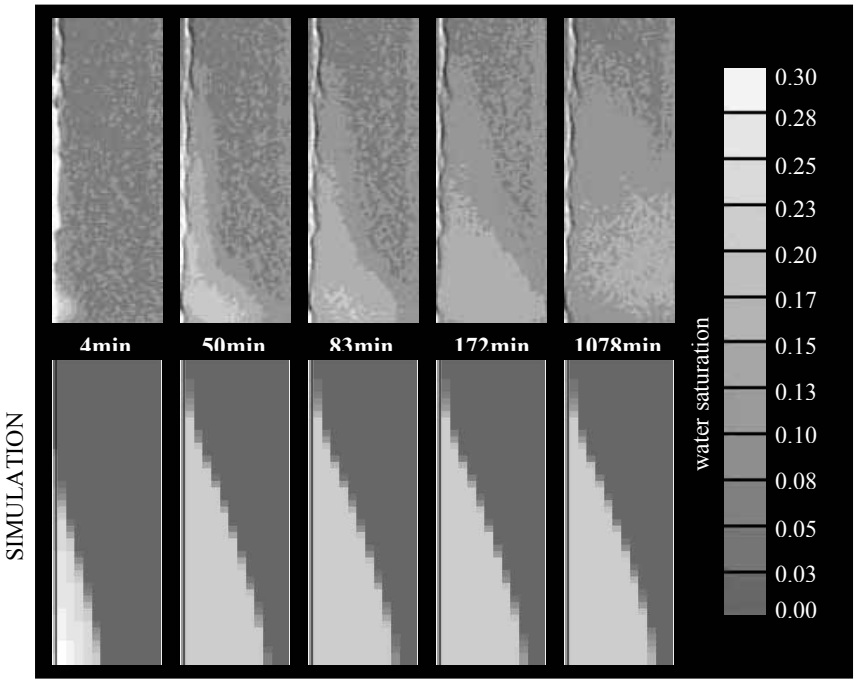


Figure 6: Simulated cumulative water front obtained from two-dimensional two-phase imbibition model.

A synthetic three-dimensional model was created using the black-oil reservoir simulator developed by CMG. The model represents a fractured system with two layers with different rock properties. Figure 7 shows the grid used to represent fracture and matrix in this model. The size of this three-dimensional system is 20x23x20 $mm^3$, with individual grid blocks of 1 x 1 x 1 mm each.

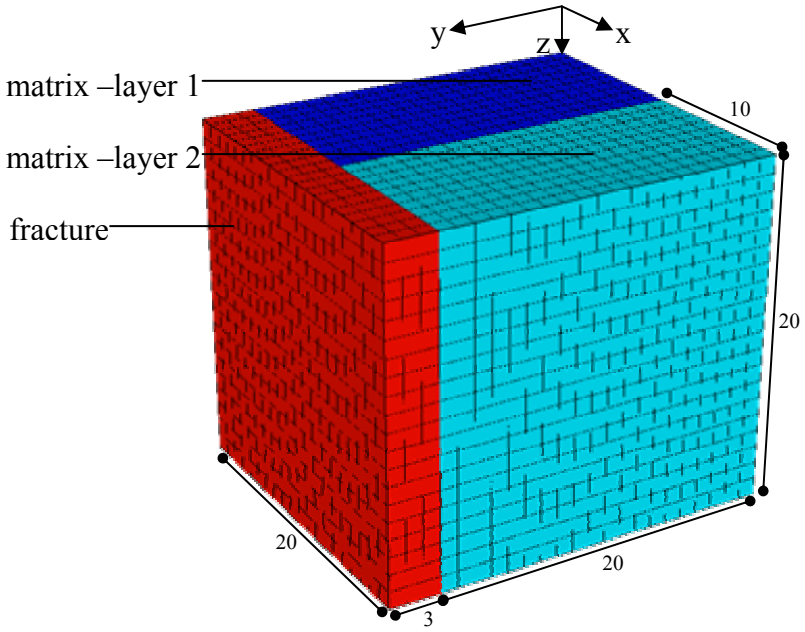


Figure 7: Grid model for simulating three-dimensional imbibition.

Rock properties used in this three-dimensional model were initially estimated from typical values found in layered Berea samples. However, those properties were later modified to enhance visualization of the flow mechanism taking place. The final rock properties used in this three-dimensional model are listed in Table 2.

Table 2: Rock properties assigned to fracture and matrix in three-dimensional model.

| PROPERTY | VALUE |
|---|---|
| Fracture permeability [md] | 500 (isotropic) |
| Matrix permeability – layer 1 [md] | 40 (isotropic) |
| Matrix permeability – layer 2 [md] | 60 (isotropic) |
| Fracture porosity [fraction] | 0.38 |
| Matrix porosity – layer 1 [fraction] | 0.12 |
| Matrix porosity – layer 2 [fraction] | 0.18 |

Different capillary pressure curves were assigned to layers 1 and 2 in the matrix. The low porosity/permeability layer (1) has higher capillary pressure values than the high porosity/permeability layer (2). Both layers 1 and 2 have higher capillary pressure values than the fracture. Figure 8 shows the capillary pressure curves used in the three-dimensional model. The drainage capillary pressure curve in each case corresponds to the upper line in the capillary loop, while the lower line corresponds to imbibition. The relative permeability curves used were similar to those presented in Figure 3

At initial conditions, the two layers in the matrix were fully saturated with oil, while water saturation increases from top to bottom in the fracture blocks. The model was subject to spontaneous mobilization of fluids and no injection took place at any time. Fracture blocks at the top of the structure have 50% water saturation, and blocks at the bottom of the sample have 100% water saturation. Experimentally, the sample had more

water available at the bottom due to upward water injection. Changes in water saturation as a function of time obtained from the three-dimensional model are presented in Figure 9. Water rapidly flows into the rock matrix, reaching farther through the low permeability layer. At early time, most fluid exchange takes place near the fracture-matrix interface, while cross-layer and in-layer flow become dominant when the fracture has drained. Figure 9 shows the development of water saturation on three faces of the model.

.

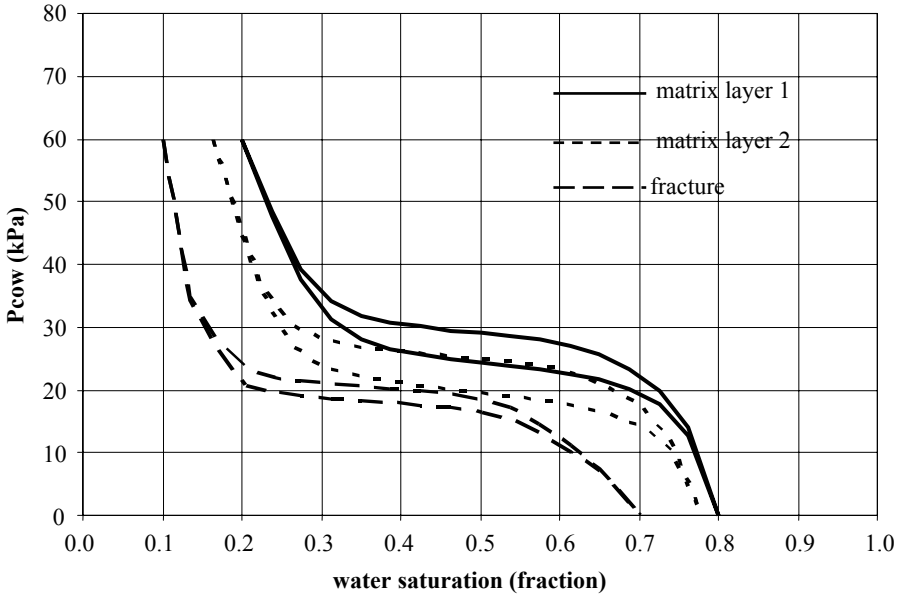


Figure 8: Capillary pressure curves used in the three-dimensional model.

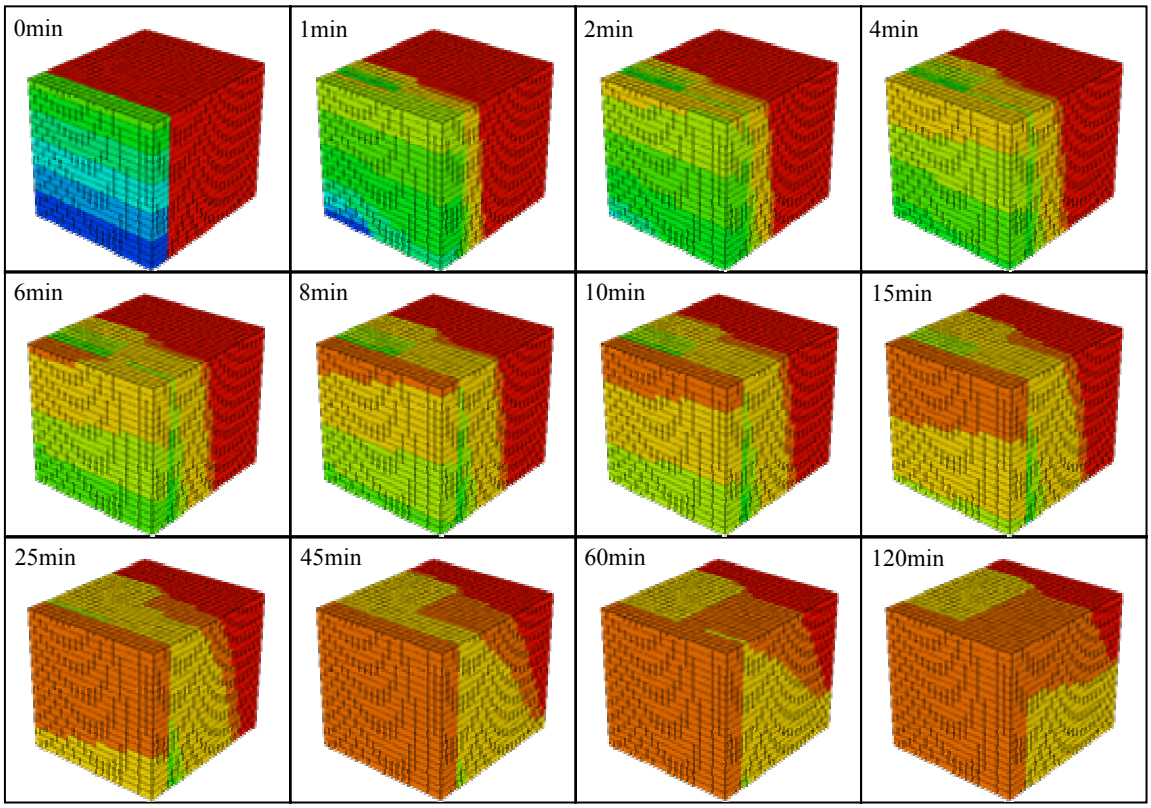


Figure 9: Changes in water saturation during capillary imbibition obtained from three-dimensional model.

Different cross-sections of the three-dimensional model were analyzed individually. Figure 10 shows the x-y or axial cross-section with the corresponding water saturation changes. The axial plane was located at z=11, penetrating the two matrix layers and perpendicular to the fracture plane. The axial cross-section shows rapid water advance through the low porosity/permeability layer and a smooth transition of the water front between the two layers.

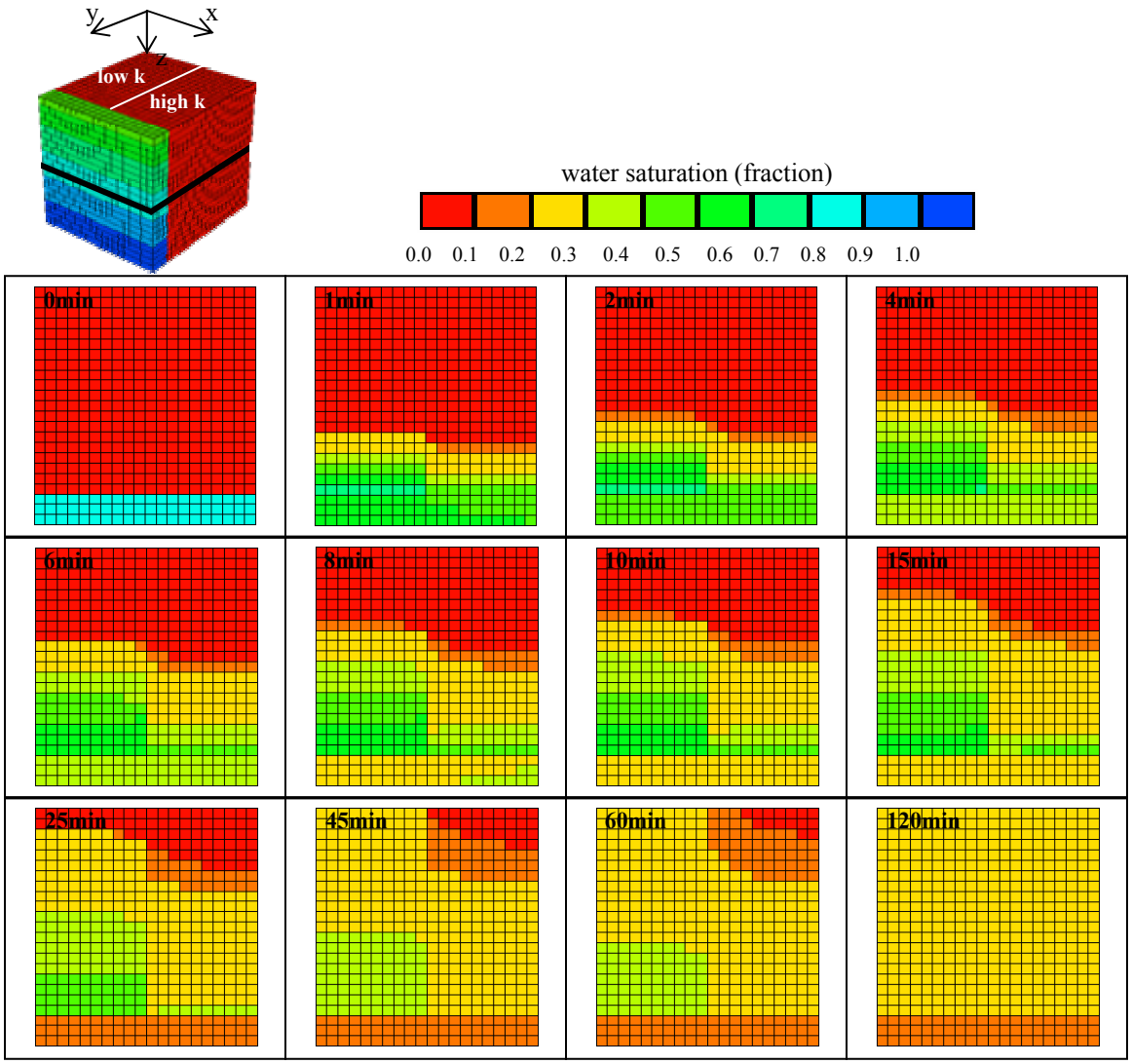


Figure 10: Water saturation changes in an axial cross-section, slice 11.

Figure 11 shows the same axial cross-section at two different times with velocity vectors for oil and water as they exchange places in the reservoir model. The top two snapshots have water flow vectors, while the bottom two have oil flow vectors. Water flow vectors at 4 minutes (top-left in Figure 11) are all pointing towards the matrix with an additional flow component between the two layers and with the fracture. Water preferentially flows

from the fracture into the low permeability layer (left) and then from the low to the high permeability layer (right). Water flow vectors at 90 minutes (top-right) shows the same mechanism that explains why the water front in the high permeability layer is delayed with respect to the low permeability layer. The snapshots at the bottom of Figure 11 show how the oil phase flows towards the fracture in counter-current flow with the water phase. Additionally, preferential flow of water through the low permeability layer pushed the oil ahead of the imbibing front, which returns in a cyclic motion through the high permeability layer and to the fracture.

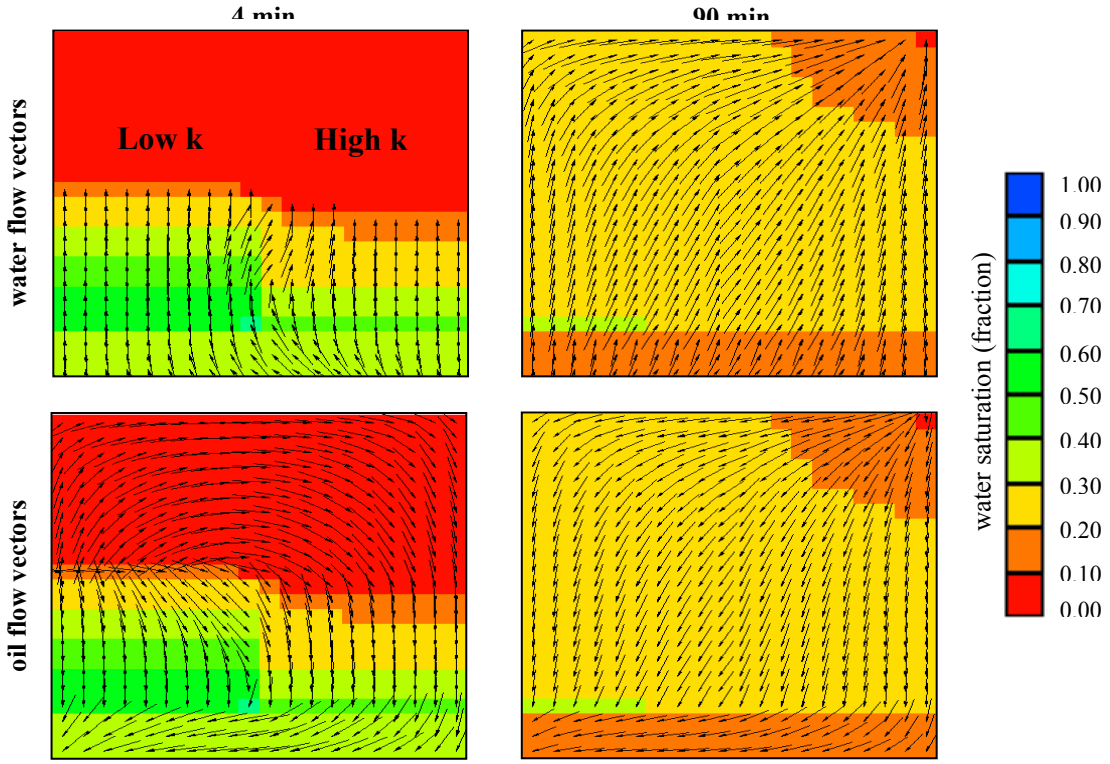


Figure 11: Water and oil flow vectors on axial cross-section at 4 and 90 minutes, slice z=11.

The simulated axial cross-sections confirmed important experimental observations explaining the mechanism of water imbibition in a fractured system with two matrix

layers (see items 1 and 3 in Figure 3). Figure 12 shows the x-z or coronal cross-section with the corresponding water saturation changes. The coronal plane was located at y=11, penetrating the two matrix layers and parallel to the fracture plane. The coronal cross-section at 4 minutes shows the arrival of the imbibing front through the low permeability layer (left). Fluid equilibration becomes slower with time due to smaller saturation gradients driving the flow mechanism.

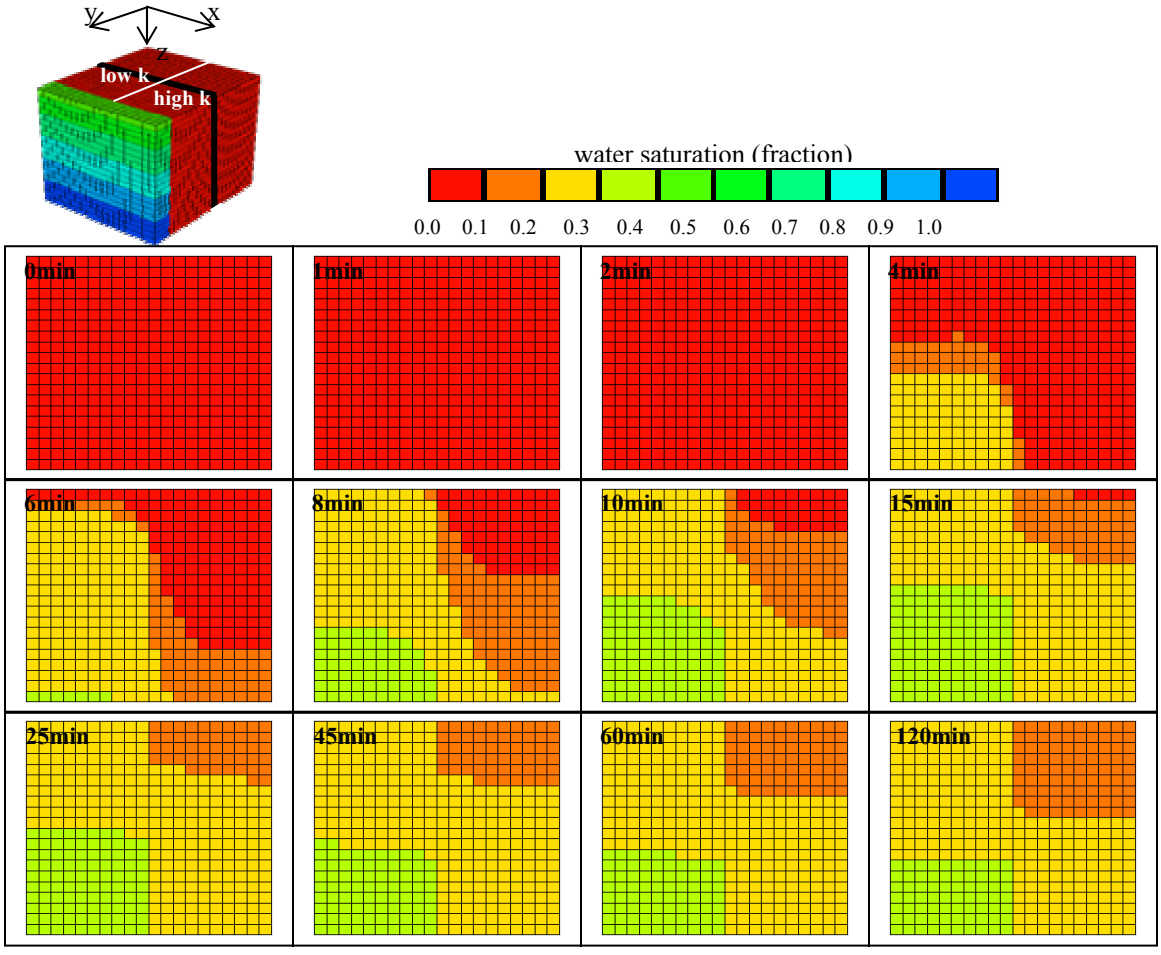


Figure 12: Water saturation changes in a coronal cross-section, slice y=11.

Figure 13 shows the same coronal cross-section at two different times with velocity vectors for oil and water as they exchange places in the reservoir model. The top two snapshots have water flow vectors, while the bottom two have oil flow vectors. The coronal cross-section confirms preferential water advance through the low permeability layer in the 4-minute image. Images at 90 minutes (top- and bottom-right) also confirm the inter-layer exchange observed in previous axial cross-section. Water preferentially flows from the fracture into the low permeability layer (left) and then from the low to the high permeability layer (right), while the oil phase flows in the opposite direction towards the fracture.

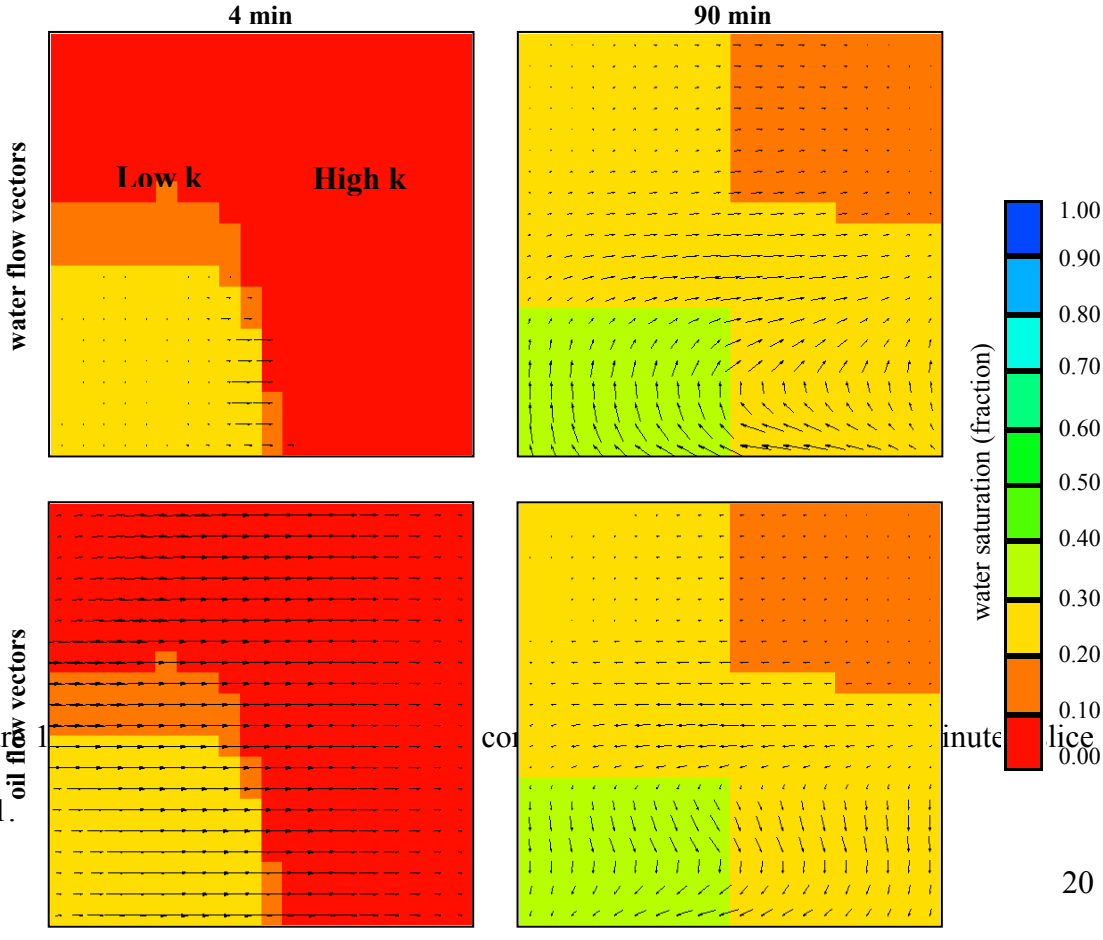


Figure 1 co inute lice y=11.

Figure 14 shows the y-z or sagital cross-section with the corresponding water saturation changes. The sagital plane was located at x=11, which extends through the interface between the high- and low- permeability layers (on the high permeability side) and is perpendicular to the fracture plane. The sagital cross-section reveals the tendency to equilibrate saturation distributions in the vertical direction at late times. The water saturation front flattens and rises at low rate in images at 45, 60, and 120 minutes.

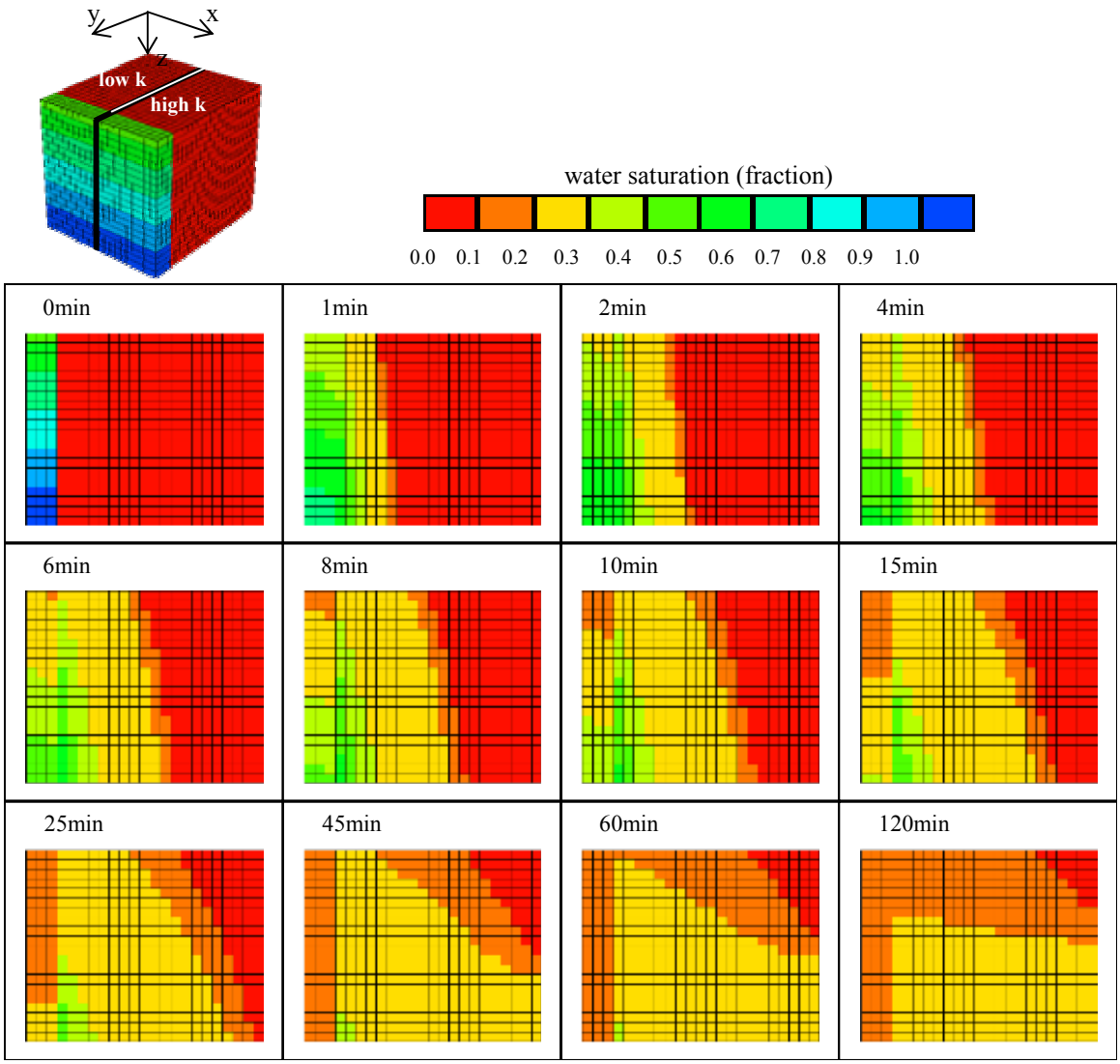


Figure 14: Water saturation changes in a sagital cross-section, slice x=11.

Figure 15 shows the same sagital cross-section at two different times with velocity vectors for oil and water as they exchange places in the reservoir model. The top two snapshots have water flow vectors, while the bottom two have oil flow vectors. The image at 90 minutes with water vectors (top-right) shows water migration away from the fracture and up with water flowing from the bottom of the sample and adjacent to the fracture. This observation corresponds to the experimental analysis made on the incremental water saturations obtained from digital radiography at $\Delta t$=15 hr and 6 min. At late time, the highest water saturation is found at the bottom of the sample. Capillarity drives this water towards regions with low water saturation at the top of the sample and away from the fracture. Simultaneously, oil migrates towards the bottom of the sample to replace the volume previously occupied by water. The simulated sagital cross-sections confirmed important experimental observations explaining the late-time longitudinal mechanism of water imbibition (see items 2 in Figure 1).

Experimental and simulated saturation profiles are presented in Figure 16. These profiles were computed from saturation changes in the axial cross-section of the three-dimensional model in order to compare with those obtained experimentally. Each millimeter in the "distance" axis (top-graph) corresponds to a grid block along the "y" direction on the axial cross-section. As time proceeds, regions near the fracture-matrix interface undergo drainage, while regions away from the fracture undergo imbibition. The lower portion of the curves moves from high water to low water saturation (drainage), while the upper portion of the curves moves from low water to high water saturation (imbibition). The transition zone between drainage and imbibition moves away from the fracture as the water front advances. The path of transition zones is

described by the locus of intercepting points between two consecutive saturation profiles. Even though the three-dimensional simulation exercise described in this document is not a replica of the experimental sample or conditions, it captured the overall mechanism of capillary imbibition experienced in the laboratory.

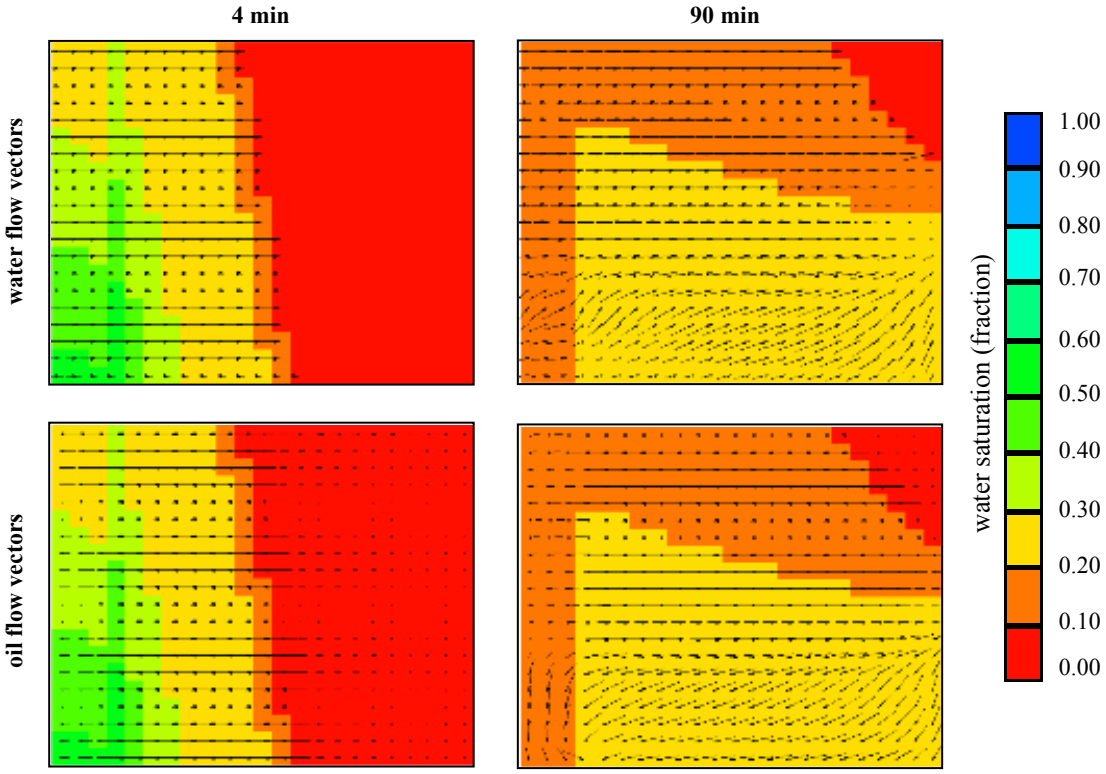


Figure 15: Water and oil flow vectors on sagital cross-section at 4 and 90 minutes, slice x=11.

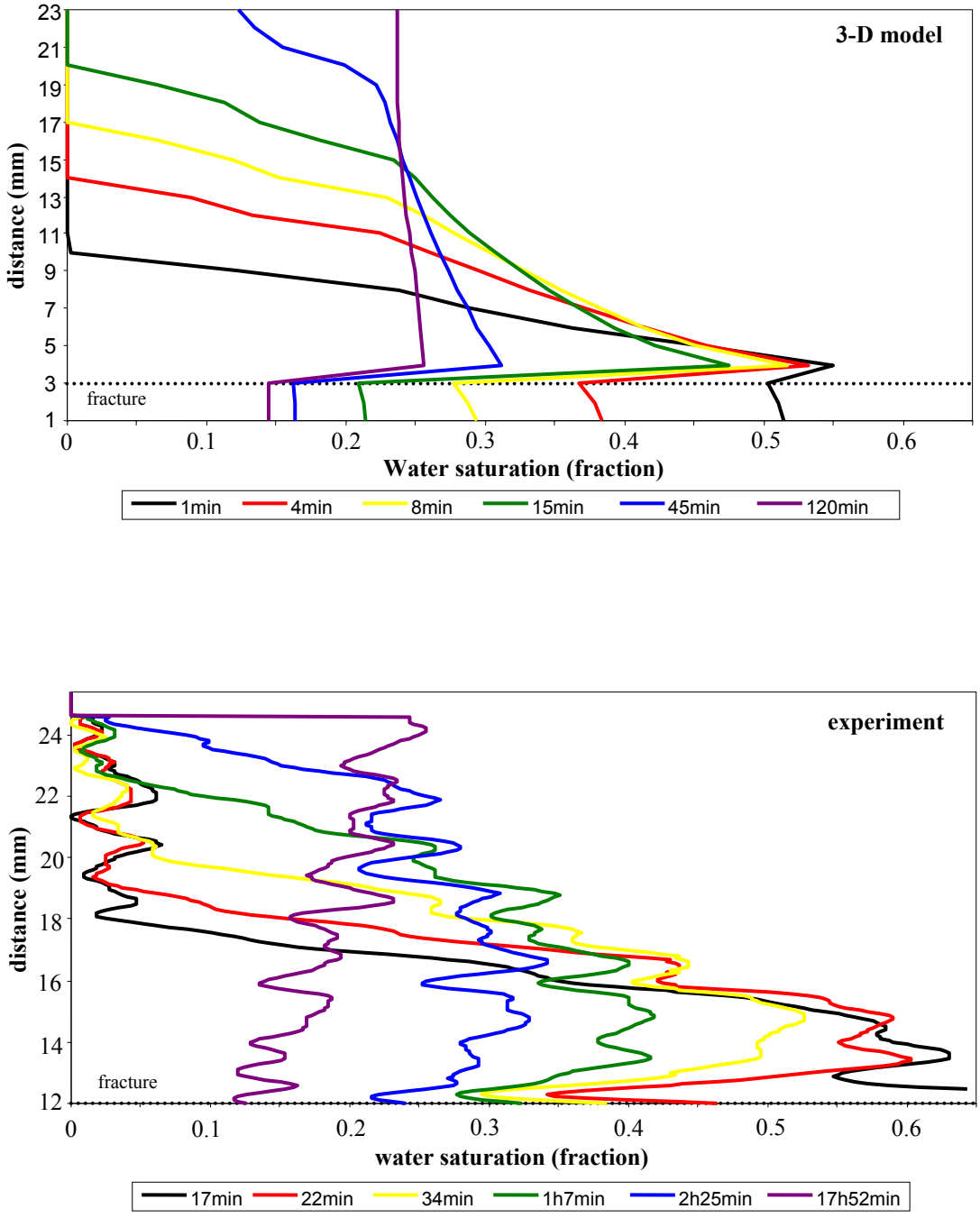


Figure 16: Qualitative comparison of cumulative water saturation profiles obtained from three-dimensional simulation and the experiment.

## CONCLUSIONS

The present work proved the ability to detect different fluid phases coexisting in a fractured rock and to obtain detailed three-dimensional fracture structures. Experimental results indicated that it is possible to characterize fracture's complex geometry and fluid phase distribution from CT data. Findings from this work contribute to correlation of multi-phase fluid conductivity with fracture geometry and wettability, which could significantly enhance current interpretation and modeling of capillary-driven flow in fractured systems. Using the experimental methods and modeling described in the present work, the following conclusions are made.

- A direct correlation between rock bedding porosity and local fracture apertures was confirmed. Large apertures correspond to layers of high porosity in the matrix, and vice versa. The separation of individual grains after fracturing is a possible explanation for this phenomenon. High porosity layers are typically well sorted, and have less inter-granular contact and weaker cementation than low porosity layers, thus stimulating larger apertures when fractured. This correlation plays an important role in controlling mass transport between the rock matrix and the fracture.

- There is a strong correspondence between fluid distribution and fracture geometry. The non-wetting phase tends to occupy large apertures, while the wetting phase spreads through small cavities. Due to this correspondence, it is possible to map fluid occupancy in a fracture from geometric data and wetting characteristics.

- Trapping of the non-wetting phase always occurs in local maxima with sufficient associated fracture volume which are surrounded by smaller apertures. An important consequence of fluid trapping is a high value of residual saturation of non-wetting phase, which makes the mobile region of the relative permeability curves narrower than those characteristic of matrix flow.

- Co-current and counter-current flow mechanisms coexist during capillary imbibition of a fractured rock originally saturated with non-wetting phase. Non-destructive monitoring of fluid flow in fractured samples allowed visualization of localized co-current and counter-current flow. The presence of saturation banks during capillary imbibition suggests that there is counter-current flow of wetting and non-wetting phases.

- Two-dimensional numerical simulation of capillary imbibition experiments demonstrated that counter-current flow prevails in the direction perpendicular to the fracture surface, while co-current flow dominates longitudinal imbibition, parallel to the fracture plane. Flow communication across layers also obeys the coexistence of co-current and counter-current flow.

- Accounting for capillary forces in the fracture is essential for successful modeling of fracture-matrix flow. Contact areas in the fracture provide passages under strong capillary action, which are able to drive wetting fluids into the rock matrix. Such behavior can be captured by means of fracture capillary pressures and void structure. For

most part of the mobile saturation window, matrix capillary forces are higher than those in the fracture. Water available to the fracture immediately reaches for the narrowest gaps and imbibes the rock matrix near contact areas. Fracture capillary forces are especially important when the rate of injection is close to or less than the rock's capacity to transport fluids.

- The presence of bedding planes in the rock's structure determines the shape of the imbibing front. The imbibing front advances faster through low porosity/permeability layers due to higher capillary forces. Low porosity/permeability regions in the rock tend to coincide with the narrowest fracture gaps where water is predominantly available after water injection thus promoting advance of the imbibing front into the rock. Cross-layer fluid exchange tends to level the imbibing front.

## SHEAR FRACTURES – PARALLEL TO BEDDING

### INTRODUCTION

Many hydrocarbon reservoirs are naturally fractured. Fluid flow patterns and hydrocarbon recovery are greatly affected by the fractures. Fractures can have positive effects on the recovery process by increasing the permeability. Fractures might have negative effects when they form bypass paths, especially in production-injection systems. Injected fluid may preferentially flow through the fractures leaving behind inaccessible hydrocarbons thus increasing the residual oil saturation. Fractures can also act as no-flow reservoir boundaries.

Two basic types of fractures are commonly observed. These types are tensile and shear fractures. Shear fractures occur when the shear stresses are greater than the strength of the formation. Shear stresses may result from tectonic activity or be induced by the presence of the well itself. It results in the formation of a surface of rupture where the shear stresses are maximum, followed by release of shear stresses as the rock suffers a displacement along the ruptured surface.

To maximize the production from fractured reservoirs, a large number of variables needed to be investigated to clearly understand the effects of shear fractures on fluid flow. Unlike tensile fractures, multi-phase flow in shear fractured reservoirs was not studied enough in the past.

**Background:** The literature discussing the effects of shear fractures on fluid flow is very sparse when compared to that discussing the effects of tensile fractures because of the need to account for the creation of a damage zone associated with shear fracture.

Makurat *et al*. (1985) studied the effects of shear deformation on the permeability of natural rough joints. The experimental results showed significant increase in the conductivity with shear displacement. However when Tuefel (1987) investigated the effects of shear deformation on the permeability of fractured rocks, he found that the permeability decreases with increasing shear deformation. This decrease in permeability is hypothesized to be due to gouge formation and pore volume compression.

Barton *et al*. (1985) developed a new model to simulate stress- and size-dependent coupling of shear stress, displacements, and conductivity, and of normal stress, closure and conductivity, he found that Smooth joints in weak rocks close most readily under normal stress, and display low shear strength and weak coupling between shearing and conductivity, on the other hand rough joints in strong rocks close least under normal stress, and display high shear strength and strong coupling between shearing and conductivity. Essaki *et al*. (1990) investigated the change of hydraulic conductivity of rock joints due to the coupled effect on joint shear deformation and the increase in volume of the rocks prior to failure "dilatancy". The result of this study indicated that the change in the hydraulic conductivity is approximately similar to that of its dilatancy. Increased deviation from the Barton model, developed in 1985, was observed with increasing shear displacement. Essaki explained this deviation to be due to gouge material produced during the shear displacement which will block part of flow paths and decreasing joint conductivity.

Olsson and Brown (1993) evaluated normal and shear offset effects on fluid flow rate. Their results showed that if the shear stress is strong enough to cause slip on discrete fractures, then significant changes in the fluid permeability is expected. Also, if the fracture surfaces are initially well matched, then the permeability will significantly increases and if the surfaces are initially poorly matched or misaligned then a decrease in permeability may be observed

Gentier *et al*. (1997) investigated the effects of shearing directions and injection pressure on the directional anisotropy of the flow for a given normal stress. This study showed that the flow direction was noticeably modified due to the shearing. Also, it showed that, for small displacements, the transmissivity of a facture depends on the shear direction.

Gentier *et al*. (2000) studied the influence of fracture geometry on shear behavior. The mechanical response of samples with the same fracture geometry to a variety of shear conditions was studied. Profiles of fracture surfaces were measured before and after shearing, and images of sheared surfaces were analyzed to quantify the damage that occurred during shearing. The results of this study indicated that the mechanical behavior for fractures under shearing stress is strongly related to the geometry of the fracture surfaces. The experimental results were used to develop an image-analysis-base algorithm to predict the location of the damage during shearing in a given direction.

The most recent study was done by Mohammed (2004). In this study the author investigated the effects of an artificial shear fracture on two-phase flow in layered Berea sandstone. The shear fracture was induced perpendicular to the bedding planes. Absolute permeability was measured before and after fracturing. Sequences of flooding tests were applied to complete this study. Two-phase flow data were acquired in the

shear fractured porous media. X-ray CT data were applied to characterize the morphology of rock matrix and the shear fracture. The results of this study indicated that the absolute permeability increases by about 80% after shearing. The study also indicated that the fracture has a few large-porosity voids. The fracture was representing 0.2% of the total sample volume. The sweep efficiency is better at the inlet than at the outlet part of the core sample

Except for Mohammed (2004), almost none the previous studies discussed the effects of a shear fracture on permeability and fluid distributions in multi-phase flow experiments. Many parameters have to be examined to understand the effects of shear fractures on multi-phase flow. Gouge formation, morphology of the fracture surface and geometry of the void spaces, effects of confining pressure, effects of displacements, effects of temperature, type of rocks are examples of the parameters to be considered in future work to understand shear fracture and hopefully to maximize the production from the fractured reservoirs.

**Objectives:** The goals of this study are:

a- Compare the change in absolute permeability due to shear fractures induced in samples cut perpendicular and parallel to bedding planes
   - Comparing fracture morphology in both cases; parallel and perpendicular

b- Map fluid distributions in 2-phase liquid system at $S_{wirr}$ and $S_{or}$ saturation conditions.

- Correlate with $k_{ro}$ at $S_{wirr}$, and $k_{rw}$ at $s_{or}$.
- Compare $k_{ro}$ and $k_{rw}$ with $k_{ro}$ and $k_{rw}$ of non-fractured sample.

**Approach:** To accomplish this goal, cores of Berea sandstone cut parallel to bedding planes were loaded to failure in a triaxial cell. Absolute permeabilities were measured before and after fracturing. Single and two-phase liquid flow studies were performed in the fractured cores, using X-ray CT to map fracture morphology and fluid saturation in the fracture and the adjacent matrix.

## MATERIAL, EQUIPMENT, EXPERIMENTS

**Materials:** Berea sandstone was used to complete this study. Berea was chosen as the porous media in this study because it is used as a standard rock for the experimental work in the petroleum industry. K-1 Kerosene and 7% by weight NaI Brine were used as oil and water phases, respectively. NaI brine was used to increase the contrast between oil and water phases. A heat shrinkable teflon tube was used to keep the sample together after the introduction of the shear fracture and also act as a jacket to prevent the confining fluid from entering the sample. Cylindrical core plugs were cut parallel to the bedding planes. The samples were surface ground, then cleaned using methanol in an ultrasonic cleaner to remove fine particles that could block the pores. Samples were dried for 24 hours in an oven at 50 $^{o}$C, then, were jacketed in heat shrinkable teflon to keep the gouge and matrix intact after shear fracturing.

**Core Holder:** An X-ray transport core holder used in the experiments can hold a one inch diameter sample. It consists of a polycarbonate tube, aluminum end-plugs that have separate ports allowing injection of two fluids, and two additional ports for pressure measurements. Two aluminum end caps were threaded at the exterior to hold the end plugs in place and provide the axial stress on the sample. Figure 17 shows the core holder and its components. Details of the core holder design are given by Karpyn (2005).

Figure 17: A photograph of the un-assembled core holder.

**Pumps:** A 2-cylinders dual flow Quizix pump was used to inject the water and oil phases into the core sample. The cylinders were filled first with kerosene to complete the kerosene flood stage, and then the cylinders were flushed four times with the water before the pump was used to complete the water flood stage.

**Computed Tomography System:** X-Ray Computed Tomography has been applied in several petrophysical applications including water saturations, lithology, pore size distribution, relative permeability, rock mechanics studies, correlation of core logs with well logs, and characterization of mud invasion. X-ray Computed Tomography (CT) is a

non-destructive imaging technique that utilizes X-ray technology and mathematical reconstruction algorithms to view a cross-sectional slice of an object. This technology was introduced for the first time in 1972. Since then, there have been several generation of X-Ray CT scanners. First generation scanners used a single pencil-beam source and detector arrangement. The Second generation scanners used multiple detectors in translate configuration. This generation improved the image quality. In the third generation scanners, both source and detectors are rotating together around the object. This generation improved the speed of data acquisition. In the Fourth generation scanners, the detectors remain fixed within a ring while the x-ray source rotates around the object. Fifth generation Scanners use a stationary-geometry method in which both the source and the detectors are fixed.

The intensity of a beam of x-ray passing through an object will be attenuated due to absorption and scattering. This attenuation depends on the density and atomic composition of the object, and on the photon energy spectrum of the x-ray beam. As the density of the object increases the attenuation will increase. The equation of decay of intensity of an x-ray after passing the object is given by Beer's law as shown in Equation 1.

$$I / I_o = \exp(-\mu h) = \exp(-\mu / \rho)\rho h \qquad 1$$

Where,

$I_o$ is the incident x-ray intensity

$I$ is the intensity remaining after the X-ray passes through a thickness $h$

$\rho$ is the density of the object

$\mu/\rho$ is the mass attenuation coefficient

*h is* the thickness

Many researchers have applied CT technology to study fluid flow interaction between tensile and shear fractures and the matrix. Keller (1998), Montemagno and Pyrak-Nolte (1999), Alajmi and Grader (2000), Mohammed (2004), and Karpyn (2005) are examples of researchers used different generations of the CT technology.

The high-resolution OMNI-X X-Ray CT Scanner at Penn State's Center for Qualitative Imaging was used to visualize the fracture morphology and the fluid distribution and its path during the experiments. The axial positioning table can move between the x-ray source and the detector to change the magnification of the object on the image intensifier. The micro focus x-ray source uses up to 225 kV at a maximum current setting of 1 mA. The x-ray sources produce cone-shaped beams that allow the collection of volumetric data. The maximum resolution of 5-10 microns can be produced with the micro-focus x-ray tube. Data can be collected at various numbers of views during scanning to optimize resolution.

**Experiments:**

**Permeability Measurements:** The absolute permeabilities of the selected samples were measured before and after fracturing. First, air permeability was measured using a commercial air permeameter. Permeability was measured by mounting the sample in the Hassler-type core holder under 0.69 MPa (1000 psig) confining pressure. Different flow rates were applied while recording Inlet and differential pressures. The absolute permeability was calculated including the Klinkenberg effect.

**Porosity Measurements:** Because a dry scan was required for the sample used in the fluid flow experiments to get the fracture morphology, we could not use the same sample to measure the porosity. Three samples adjacent to the sample used in the fluid flow experiments were selected to measure the porosity. Length, diameter and dry weight were recorded for each sample to be used in calculating bulk and pore volumes. All samples were put in a rounded bottom flask and vacuum was applied (25 μ). Then distilled water was introduced to the samples. The samples were left for one hour under the water and then the wet weights were recorded. Porosity was calculated using Equation 2**.** Figure 18 shows the experimental setup to measure the porosity. Table 3 shows the porosity values for the three selected samples.

$$\phi = \frac{(W_{wet} - W_{dry})\rho}{VB} 100 \qquad 0$$

Where:
$\phi$ = porosity, %
$W_{wet}$ = wet weight of the sample, g
$W_{dry}$ = dry weight of the sample, g
$\rho$ = density of the distilled water, 1 g/cm$^3$
$VB$= Bulk volume of the sample, cm$^3$

The average porosity of the three cores was 18.46 %.

Figure 18: The experimental set-up for porosity measurement.

Table 3: Basic properties of porosity-test samples.

| Sample | L | D | A | BV | $W_{dry}$ | $W_{wet}$ | PV | $\phi$ |
|---|---|---|---|---|---|---|---|---|
| # | cm | cm | $cm^2$ | $cm^3$ | Gm | gm | $cm^3$ | % |
| 1 | 7.21 | 2.54 | 5.06 | 36.49 | 77.28 | 83.90 | 6.62 | 18.14 |
| 2 | 7.74 | 2.54 | 5.06 | 39.20 | 82.38 | 89.72 | 7.34 | 18.72 |
| 3 | 7.45 | 2.54 | 5.06 | 37.73 | 79.95 | 86.94 | 6.99 | 18.53 |

**Inducing the Fracture:** Selected Berea Sandstone sample was mounted in a Hoek cell. Axial force was applied to the pistons while confining pressure was maintained by a hydraulic pump. Figure 19 shows the cell before fracturing. Figure 20 shows the cell in the stress frame To eliminate the possibility of tensile fracturing, an axial load of 2.0 kN (450 pound-force) was applied to the cell before applying 10.34 MPa gauge (1500 psig) confining pressure. Differential stress was applied under constant displacement rate of 1.40 μm/sec. The vertical load gradually increased up to the point of failure. After failure, the sample was displaced an additional 500 μm to be sure that the fracture is open and connected. During the fracturing process, the load on the sample was recorded and is shown in Figure 21**.** Figure 22 shows the selected sample before and after fracturing.

Figure 19:  Cell is ready for the fracturing process.

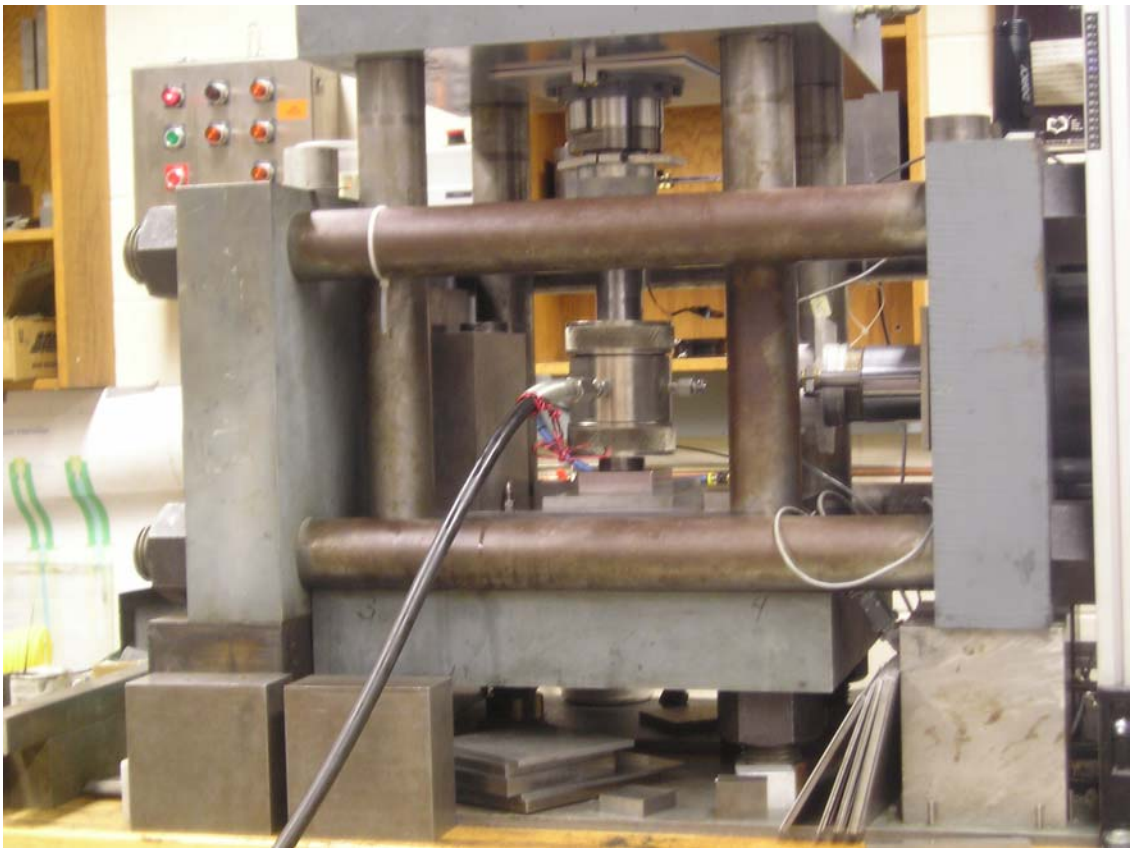

Figure 20:  Hoek cell is subjected to a vertical load.

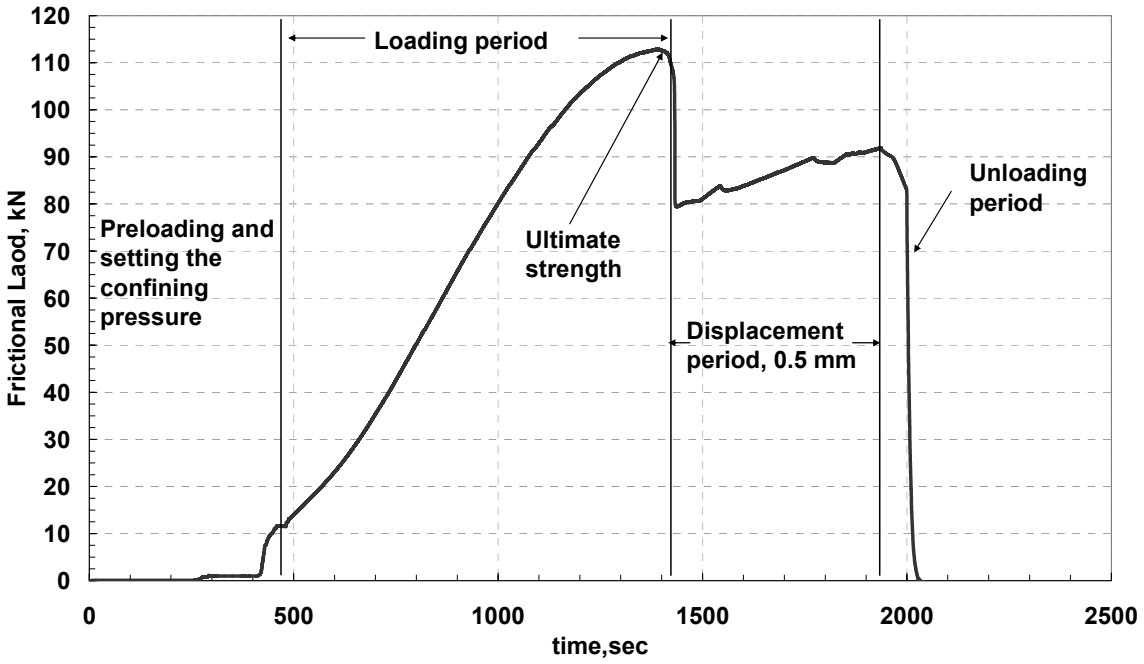


Figure 21: Typical load-displacement record showing peak stress and post-failure displacement.

Figure 22:  Fracture frame after failure and 0.5 mm of vertical displacement.

**Two-Phase Flow Experiments:** To perform two-phase fluid flow experiments, the fractured sample was mounted in the core holder (Figure 17). A second heat shrinkable Teflon tube was used to keep the sample in contact with the end-plugs and to prevent the confining fluid from leaking into the core sample. The confining pressure used was 0.2 MPa gauge (30 psig). The experiments consisted of four different stages. First, the core was scanned dry to determine the tomography of the fracture. In the second stage, the core sample was fully saturated with 7% NaI brine. To saturate the sample, vacuum (120 □) was applied at the top of the core holder. Then NaI brine was introduced to the core sample from the bottom. The sample was scanned while fully saturated with NaI brine. This scan is important when calculating water and oil saturations. In the third stage, kerosene was introduced to the sample. Kerosene has low CT signature in comparison to the NaI brine. The CT contrast between the NaI brine and the kerosene helps to visualize and analyze the displacement process. Kerosene is a strong drying agent and therefore was kept in contact with the brine in an external reservoir to maintain equilibrium and to ensure that the kerosene did not dry out the sample. About 5 pore volumes of kerosene were injected until no additional brine was produced form the core sample. The produced NaI brine was collected to determine the irreducible water saturation ($S_{wirr}$). The produced brine is 3.7 cc. The entire sample was scanned at the end of kerosene flood. Finally, the sample was again flooded with about 8 pore volumes of NaI brine to displace the oil. The sample was scanned for the final time at the end of the NaI flood. Figure 23 shows a photograph of the core holder in the scanner. Figure 24 shows a schematic diagram of the experiment set-up and the X-ray CT scanner used in this study.

Several sequences of x-ray CT scans at a voxel resolution of 30 □m were acquired. A micro focus x-ray source was used with tube voltage and current of 150 kV and 120 □A, respectively. A total of 2173 slices were collected through the core length during each flooding experiments. The slice thickness was 33.7 □m.

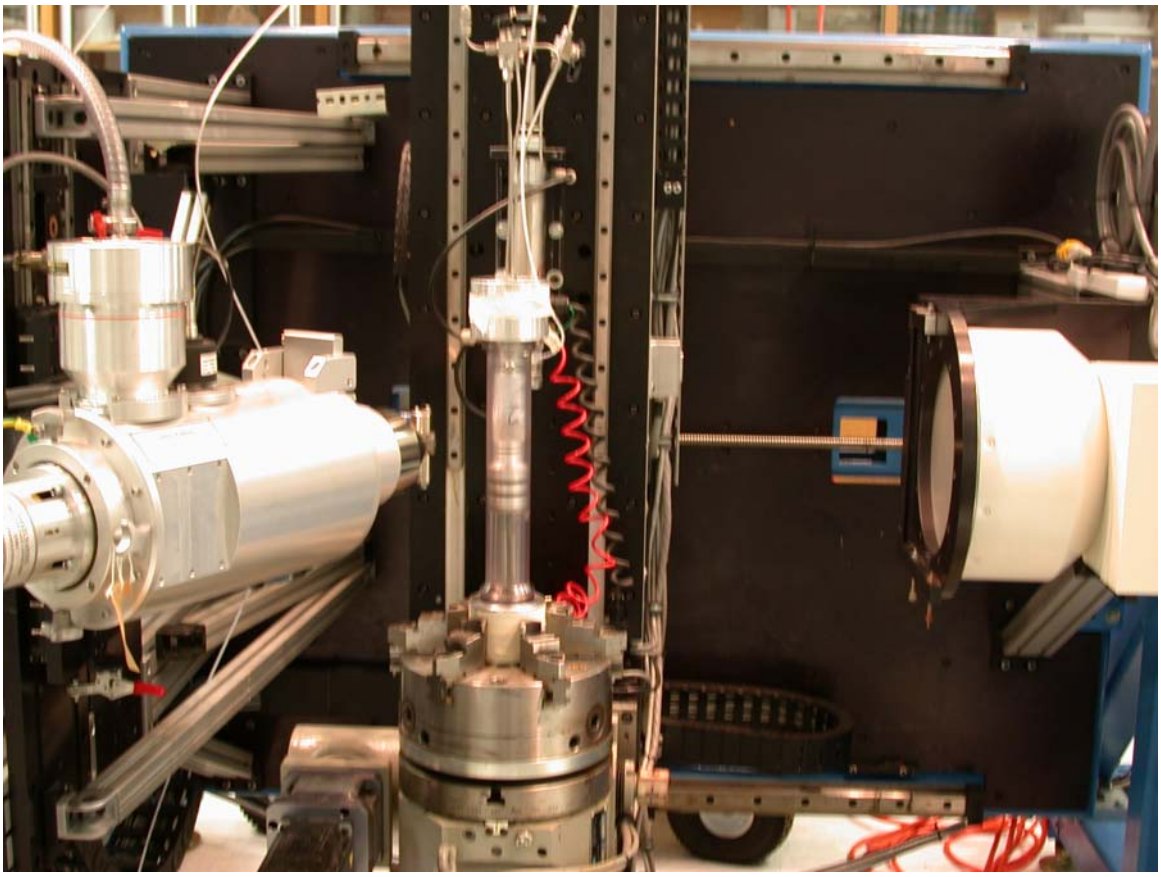

Figure 23: Photograph of the experimental set-up.

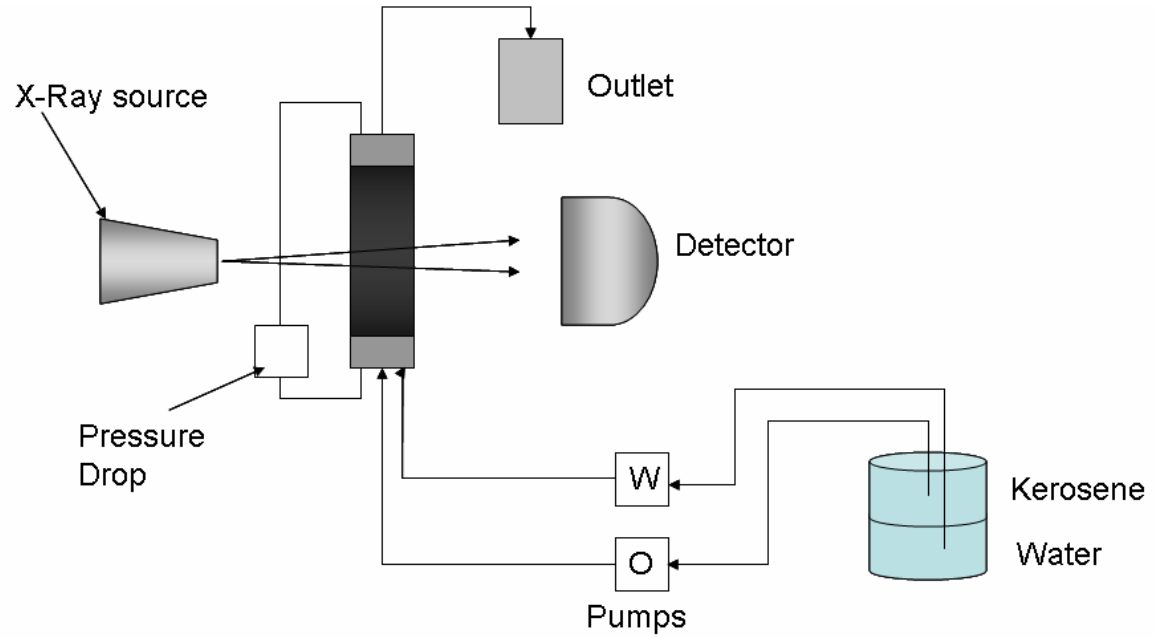


Figure 24: Schematic of the Experimental set-up.

## RESULTS AND DATA ANALYSIS

**Permeability Changes Caused by Fracturing:** Axial permeability was measured before and after fracturing using an air permeameter and Darcy's law for compressible flow as shown in Equation 3.

$$k = \frac{2Q\mu LP_s}{A(P_{in}^{\ 2} - P_{out}^{\ 2})} \qquad 3$$

Where:

k (darcy) = the permeability to air
Q ($cm^3/sec$) = flow rate
*A* ($cm^2$) = the area of the sample
μ (cp) = the fluid viscosity
$P_s$ (atm) = standard pressure (1 atm)
L (cm) = the length of the sample
$P_{in}$ (atm) = inlet pressure
$P_{out}$ (atm) = outlet pressure

To account for the slip effect in gas flow, Klinkenberg in 1941, noted that plotting air permeability versus $1/P_{(average)}$ gives a straight line. To get the absolute permeability, the data were extrapolated to $1/P_{(average)} = 0$, ( $P_{(average)}$ approaching infinity). The gas at this condition would be compressed into a liquid-like state so the extrapolated permeability is assumed to be the "absolute" permeability to liquid. Equation 4 shows the relationship between gas and liquid permeabilities. Absolute permeability was calculated for four samples before and after fracturing.

Absolute permeability was reduced by 10% to 30% after fracturing. The permeability of the specific sample (#3) used in the flooding experiment was 158.1 md

before the fracturing and 110.76 md after the fracturing. The reduction in absolute permeability is 30% after fracturing.

Figure 25 shows the permeability calculations fore the sample selected for the flooding test before and after fracturing.

$$k_g = k_{abs} + m(1/P_{ave}) \qquad 4$$

Where:

$k_g$ (darcy) = gas permeability

$k_{abs}$ (darcy) = absolute permeability

$m$ = the slope of the straight line

$P_{ave}$ (atm) = average pressure, $(p_{in} + p_{out})/2$

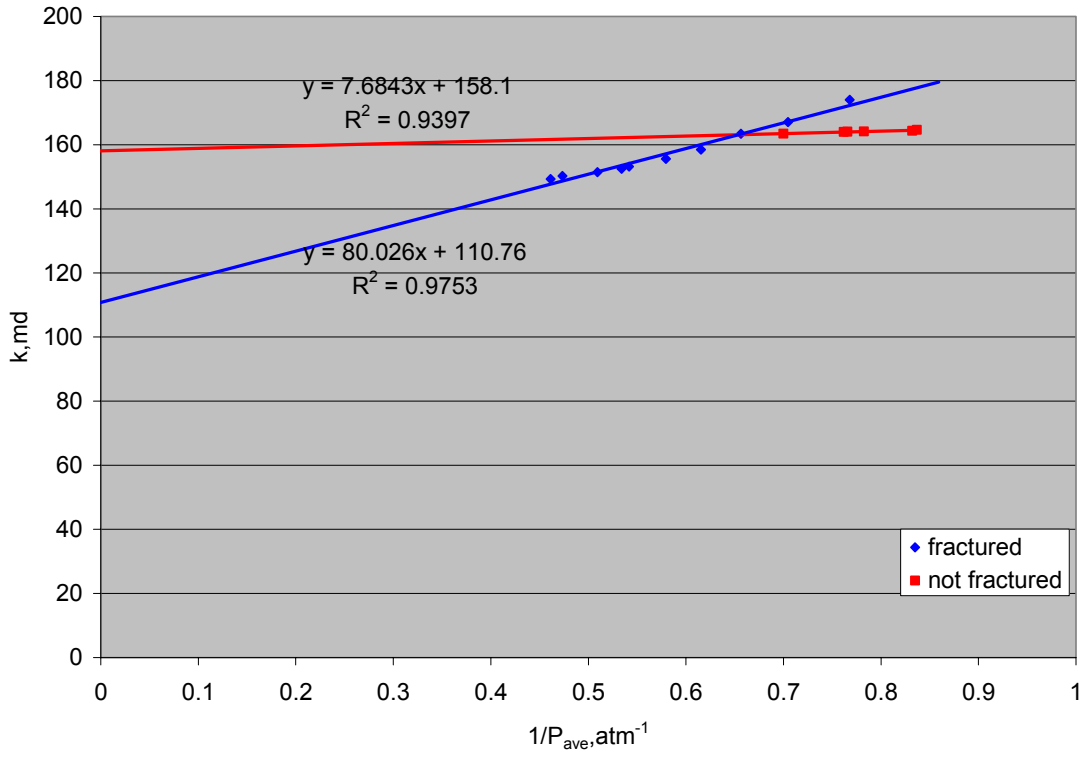


Figure 25: Permeability of the sample before and after fracturing.

Another group of samples were cut perpendicular to bedding planes. Air permeabilities of these samples were measured before and after fracturing. Air permeabilities were increased 9% to 18% after fracturing. These results are in agreement with the result reported by Mohammad (2004). The permeability results for are summarized in Table 4.

Table 4: Air permeabilities for samples cut parallel and perpendicular to bedding planes before and after fracturing.

| | Sample # | Permeability, md | | |
|---|---|---|---|---|
| | | pre-fractured | fractured | K change, % |
| Parallel | 1 | 106 | 82 | - 23 |
| | 2 | 86 | 78 | - 10 |
| | 3 | 158 | 111 | - 30 |
| | 4 | 136 | 118 | - 14 |
| Perpendicular | 1 | 77 | 84 | + 9 |
| | 2 | 67 | 77 | + 15 |

**Dry Fracture Morphology:** Fractures were extracted from the dry scan for the sample fractured parallel to bedding planes and perpendicular to bedding planes. The volumes of the fractures in parallel and perpendicular to bedding planes samples are 181.48 $mm^3$ and 111.66 $mm^3$, respectively, representing 0.75% and 0.58% of the bulk volume of the samples shear fractured parallel and perpendicular to bedding planes, respectively. The shear fracture induced parallel to the bedding planes has larger and wider distribution of the asperities than the fracture induced perpendicular to the bedding planes. Figure 26 shows partitioned maps of the fractures induced parallel and perpendicular to bedding planes extracted from dry scans.

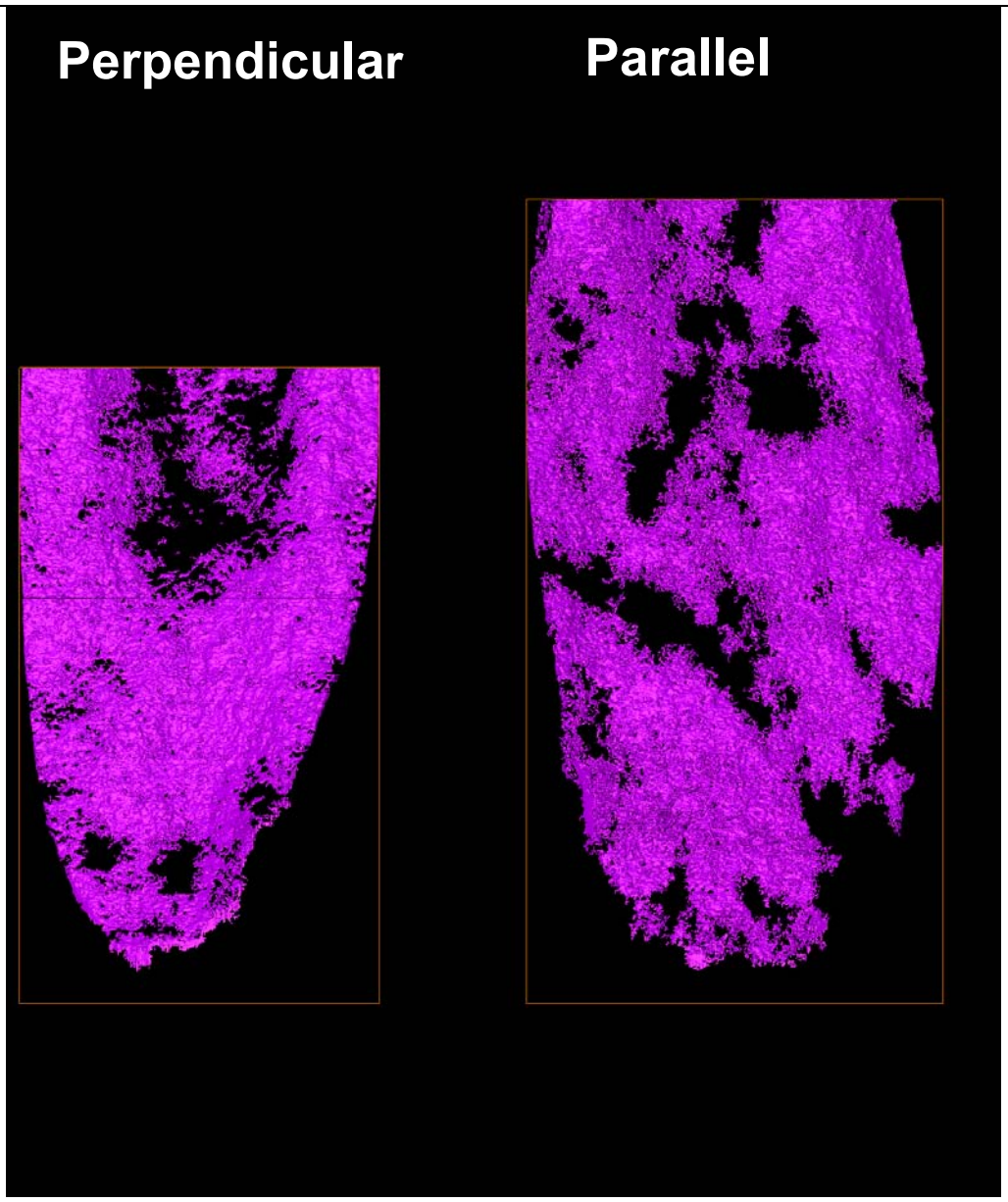


Figure 26: Binary maps of the fractures created in perpendicular and parallel to bedding planes samples.

The reduction in permeability in the parallel to bedding planes cores could be explained by the dislocation of the layers. The fracture was displaced be 500 μm.

Because the fracture was introduced parallel to the bedding planes, this displacement resulted in dislocation of the layers where the low density layer faced a high density layer and vise versa as shown in Figure 27. Layers dislocation forces the fluid to change its path, and as a result change the permeability. Another possible reason for the reduction of permeability could be the gouge formation after the introducing the fracture. The permeability of these regions in the direction of the flow is very low, thus, reducing the overall permeability. Gouge formation can not be shown directly in the fracture map extracted from the dry scan, but it will be discussed in coming sections.

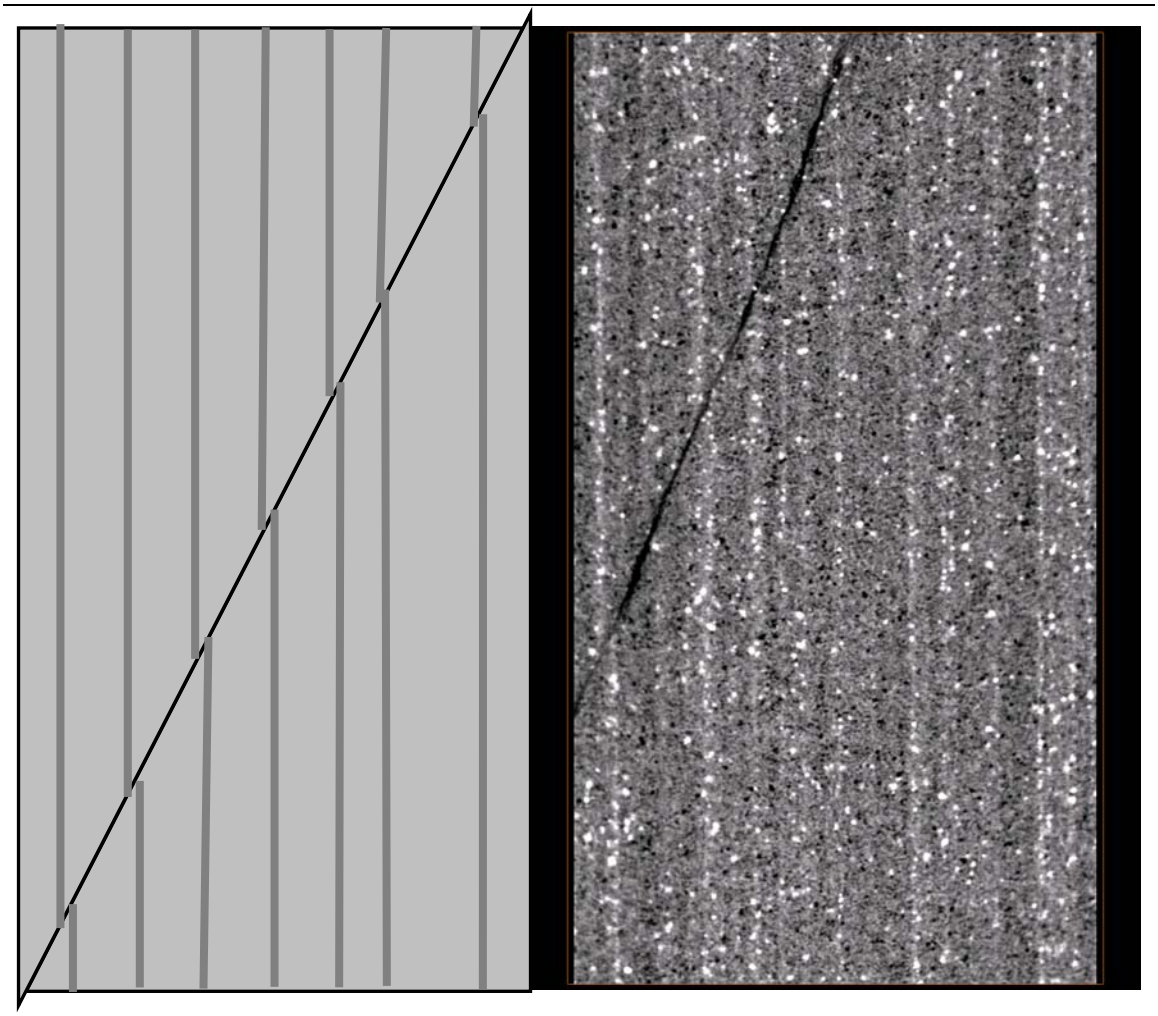

Figure 27: Schematic and actual layers dislocation after fracturing.

**Fluid Distribution in Two-Phase Liquid System:** To determine the topology of the fracture and the distribution of fluids in the sample, several computer programs were developed in PV-WAVE, preserving the spatial resolution provided by the scanner. The CT data were visualized and processed by applying VoxleCalc and Amira software packages.

The first step in analyzing CT-data was to reconstruct the slices to 256 x 256 and 1024 x 1024 matrix sizes. The second step was cutting the images to eliminate the rubber jacket. The new high-resolution slices are 822 x 822 matrices. The four stages of the experiment were: dry condition, 100 % water saturation, irreducible water saturation after an oil flood, and residual oil saturation after a water flood. Figure 28 through Figure 32 show image number 600, located at 19.6 mm from the injection end, at different stages. Figure 28 shows that the fracture is quit open in some regions, red regions, and almost close in other regions, blue region. The blue region is the possible place for the asperities and the gouge formation.

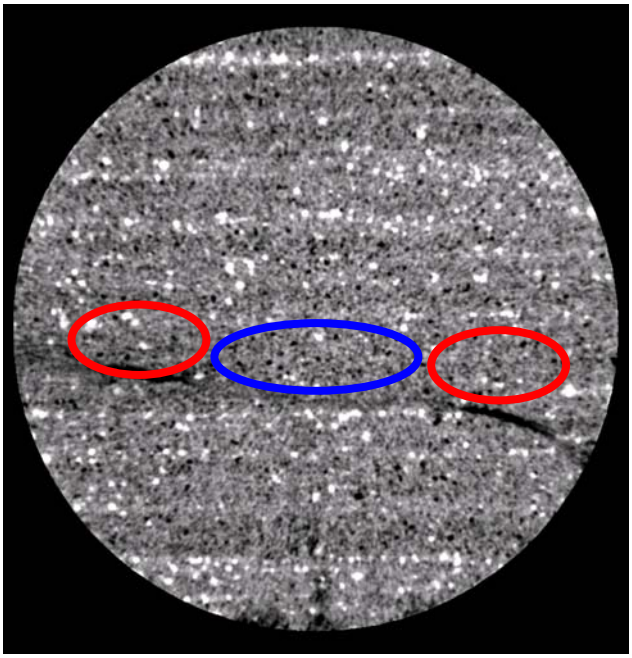

Figure 28: Example of single CT slice at dry condition. Slice number 600 located at 19.6 mm from the injection end.

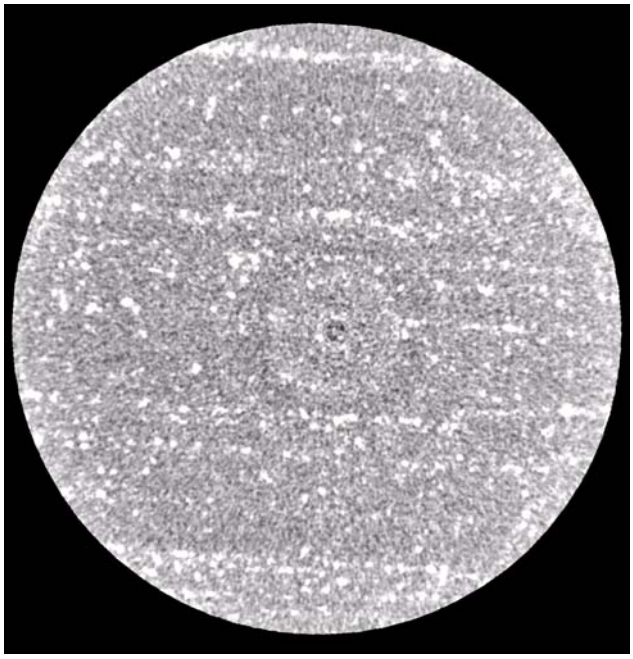

Figure 29: Example of an image of a water saturated core. Slice number 600 located at 19.6 mm from the injection end.

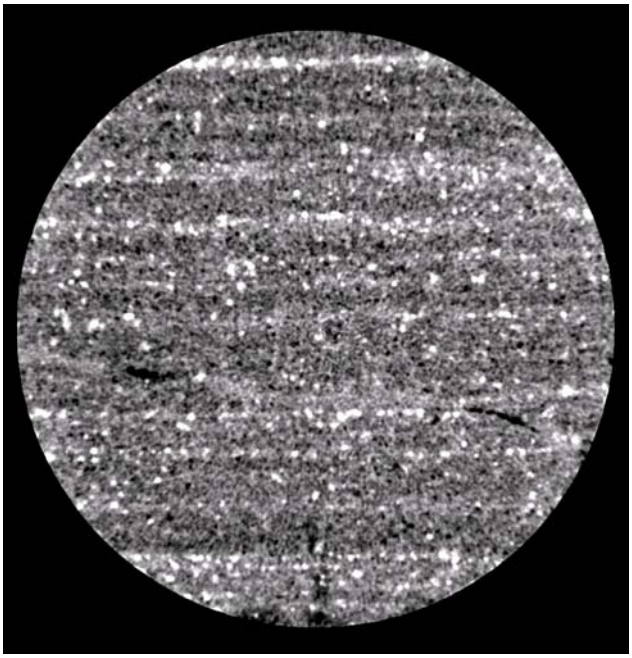

Figure 30: Example of a CT slice at irreducible water saturation, $S_{wirr}$. Slice number 600 located at 19.6 mm from the injection end.

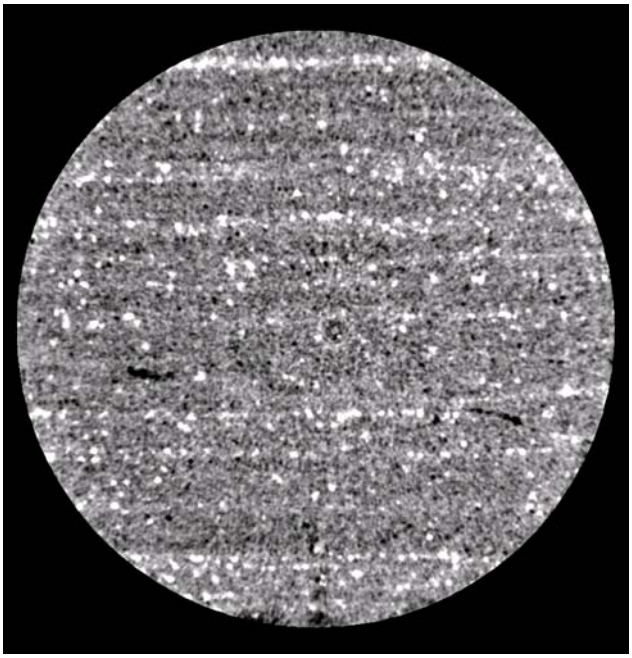

Figure 31: Example of a CT slice at irreducible water saturation, $S_{or}$. Slice number 600 located at 19.6 mm from the injection end.

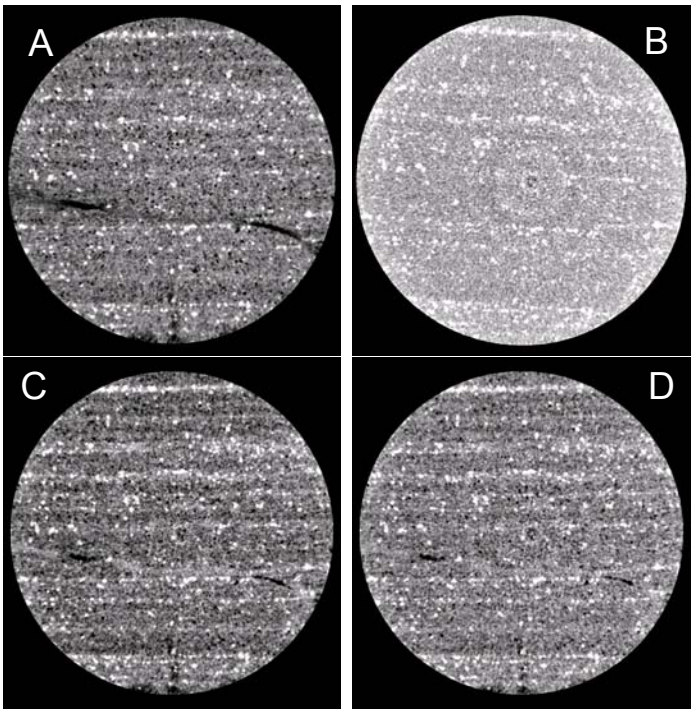


Figure 32: Example of single slice at the four experimental stages. A: Dry, B: $S_w$=100%, C: $S_{wir}$r, D: $S_{or}$.

Subtracting dry images from water saturated images yields the distribution of the water in the sample. Figure 33 through Figure 36 show the locations of the fluid at different experimental stages for slice number 600, located 19.6 mm form the inlet of the core.

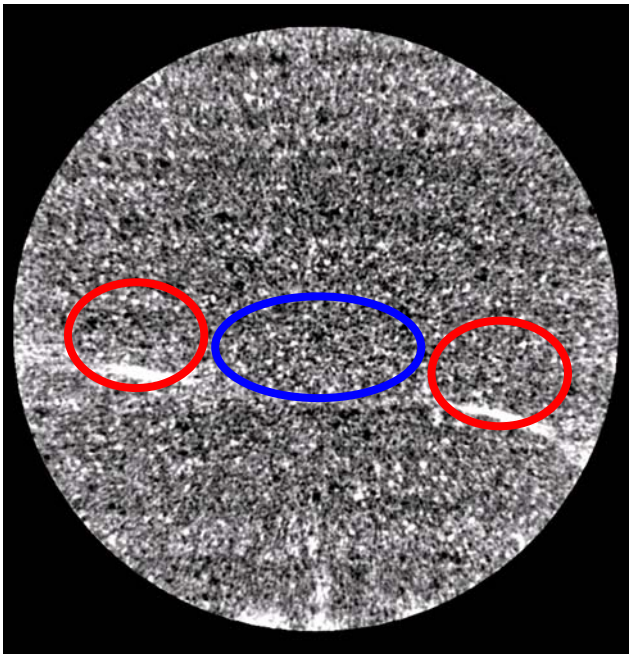

Figure 33: A single CT slice resulted from subtracting the dry image from the fully water saturated image. Slice number 600 located 19.6 mm from the inlet of the core.

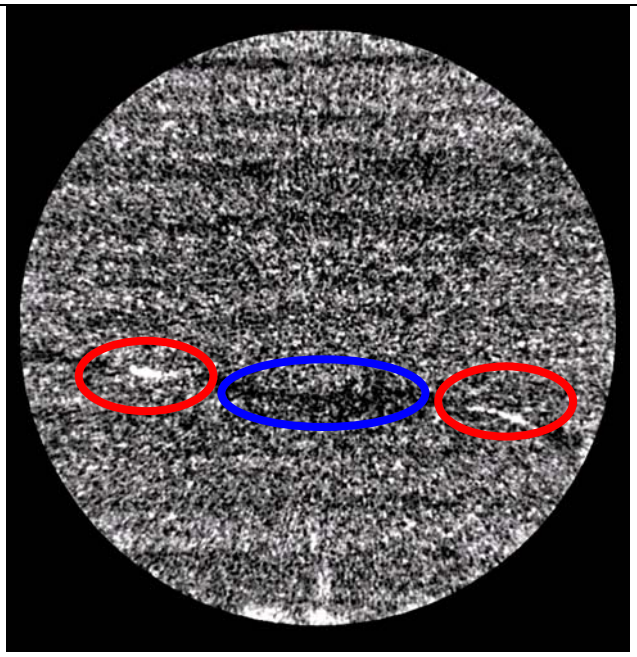

Figure 34: A single CT slice resulted from subtracting kerosene-flooded image from the fully water saturated image. Slice number 600 located 19.6 mm from the inlet of the core.

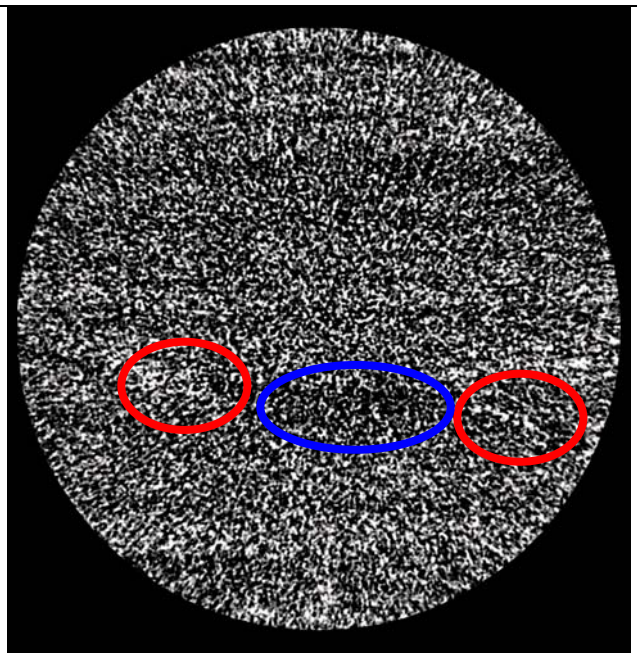

Figure 35: A single CT slice resulted from subtracting $S_{wirr}$ image from $S_{or}$ image. Slice number 600 located 19.6 mm from the inlet of the core.

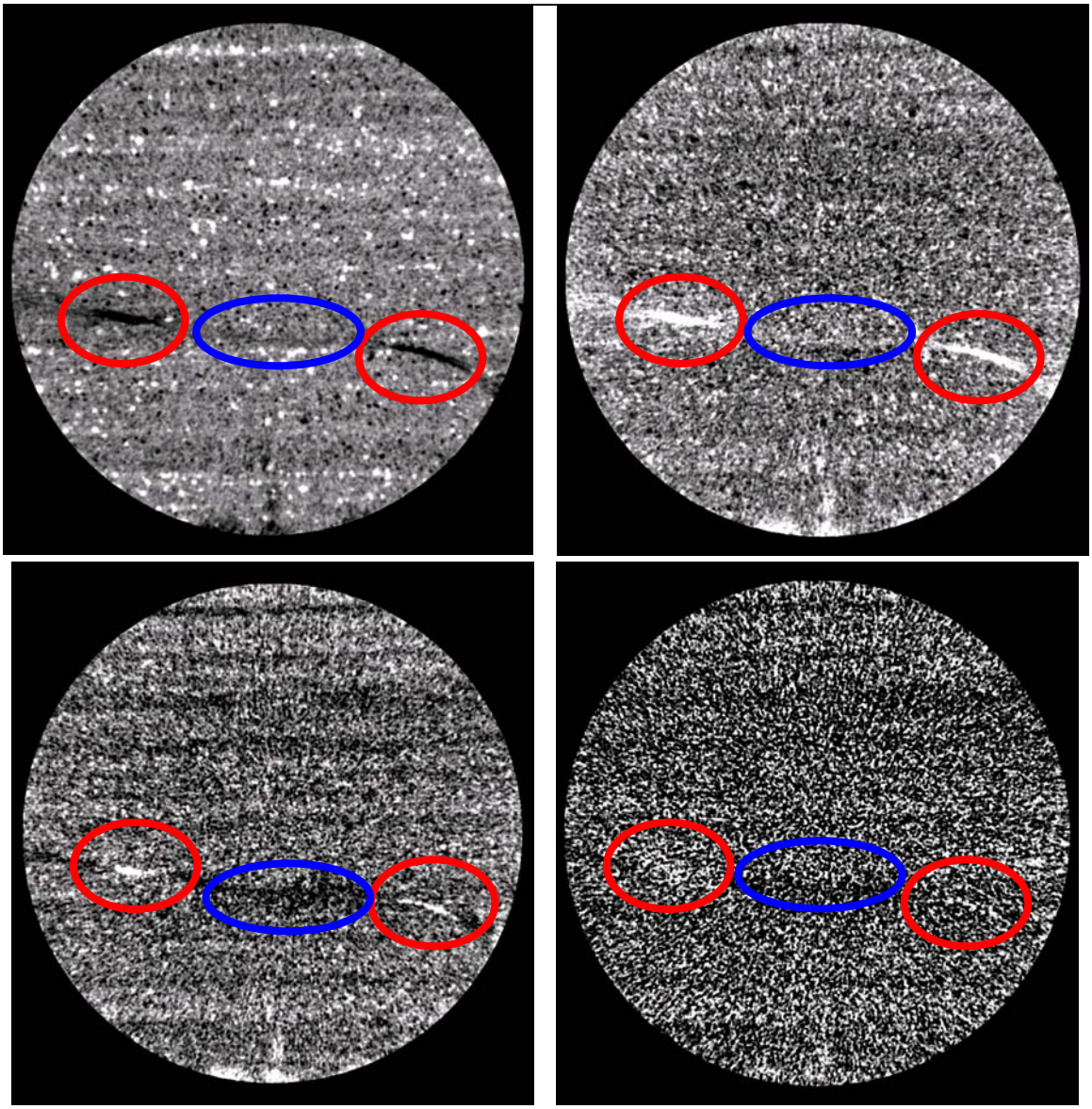

Figure 36: Slice number 600, located at 19.6 mm from the injection end, at different saturation conditions.

Figure 33 shows that the matrix and the fracture were fully saturated with the brine. The portions of the fracture that have high apertures are the dark linear features shown in Figure 28. In the subtractive image shown in Figure 33, these portions appear as the

white areas highlighted by the red ellipses. The portion of the fracture that has low apertures or may even forms asperities (the center part in Figure 26 and Figure 31) has almost the same CT signatures as the rest of the core. The blue region is possibly the gouge formation because it was saturated with water and retained this water, and it is the possible reason of the reduction in permeability as discussed in the previous section. Figure 34 shows an image after subtracting the kerosene-flooded image from the fully brine-saturated image. The kerosene resides in the open parts of the fracture, red regions, and not replaces the water in the low aperture region of the fractures. Figure 35 presents a single slice that resulted from subtracting the kerosene-flooded image from the image at the same position acquired at the end of the water flooding stage. This figure demonstrates that it is difficult to remove the kerosene out of the fracture by water displacement. The center of the open fracture is still saturated with kerosene (red). Some kerosene was removed from the open part of the fracture (red) but much less than the amount of water that was removed by the oil displacement process, Figure 33. Figure 36 presents slice number 600, located at 19.6 mm from the inlet of the core, at different subtraction steps.

These observations were supported by calculating the average CT number for each slice at different stages. Figure 37 shows that the CT number decreased after the kerosene flood. When the sample was flooded with the brine, the CT number did not change much indicating that the kerosene saturation did not significantly decrease.

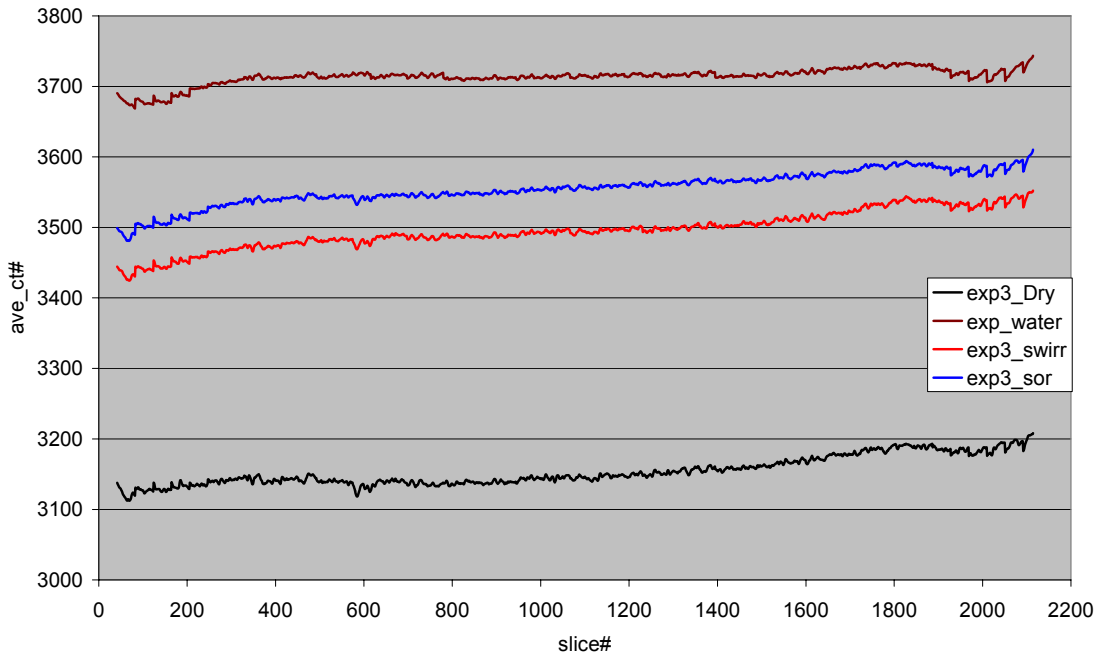


Figure 37: Average slice CT number at different stages.

**Porosity:** To calculate the average porosity for each slice, the voxel porosity was first calculated using Equation 5:

$$\phi_{voxel} = \phi_{ext}\left(\frac{\Delta CT_{voxel}}{\overline{\Delta CT}_{avg}}\right) \qquad \textbf{5}$$

Where:
$\phi_{voxel}$ = voxel porosity
$\phi_{ext}$ = average porosity measured in separate experiments, which equals 18.4%
$\Delta CT_{voxel}$ = difference in CT at each voxel (water-dry)
$\overline{\Delta CT}_{avg}$ = the difference between average CT of water and average CT of dry.

Then average porosity for each slice was calculated. Figure 38 shows average porosity for each slice. It shows that the porosity decreased at the end of the sample because this section is not fractured. Also it shows that there is a regional increase in porosity in the region highlighted by red. This increase is due to the secondary tensile fracture found in this region.

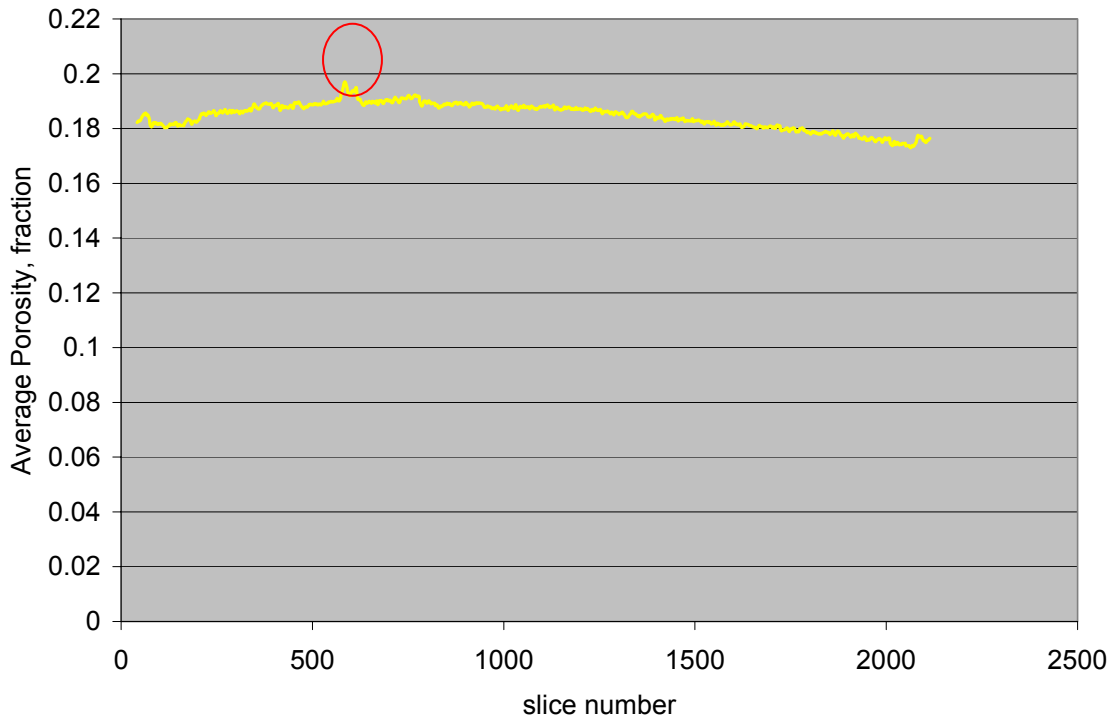


Figure 38: Average porosity of each slice.

Saturation and Relative Permeability: Water saturations at $S_{wirr}$ and sor at each voxel was calculated using Equation 6:

$$S_{w,\,voxel} = 1 - \Delta CT_{voxel}\left(\frac{1 - {}_{swirr,ext}}{\overline{\Delta CT}_{avg}}\right)\left(\frac{\bar{\phi}_{ext}}{\phi_{voxel}}\right) \qquad \textbf{6}$$

Where:

$S_{w,voxel}$ = water saturation for each voxel

$\Delta CT_{voxel}$ = difference in CT for at each voxel.

$S_{wirr,ext}$ =irreducible water saturation calculated at the end of oil flooding.

$\overline{\Delta CT}_{avg}$ = the difference between average CT of water and average CT of dry.

$\bar{\phi}_{ext}$ = average porosity measured in separate experiments, which equals 18.4%.

$\phi_{voxel}$ = porosity of each voxel calculated using Equation 5.

Average water saturations at $S_{wirr}$ and $S_{or}$ were found to be 49.1% and 64.4%, respectively. Figure 39 shows that about 15% of oil was produced from the core sample after water flooding.

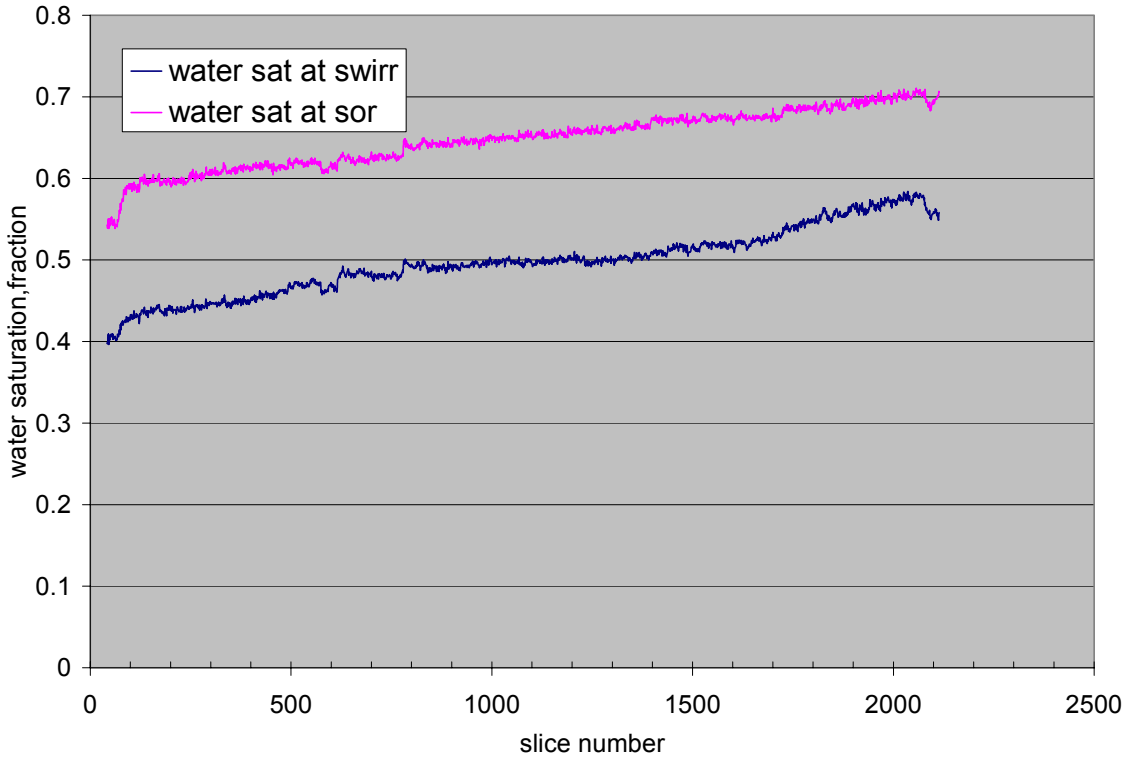


Figure 39: Average water saturation for each slice at $S_{wirr}$ and $S_{or}$ conditions.

Pressure data were collected at $S_{wirr}$ and $S_{or}$ condition. Relative permeabilities to kerosene at $S_{wirr}$ and to water at $S_{or}$ are 0.4 and 0.1, respectively. These relative permeabilities were compared to permeability values calculated for non-fractured samples at $S_{wirr}$ and sor conditions. Water saturation at $S_{wirr}$ and $S_{or}$ for non-fractured sample are 47% and 80%, respectively. Relative permeabilities to kerosene at $S_{wirr}$ and to water at $S_{or}$ are 0.89 and .09, respectively.

Saturation values for fractured and non-fractured samples show that there is not much difference in the value of $S_{wirr}$. There is a large difference in sor values indicating that oil recovery from the non-fractured sample is larger than that produced form fractured sample. Table 5 summarizes relative permeability calculations for fractured and non-fractured samples.

Table 5: Relative permeabilities at $S_{wirr}$ and $S_{or}$ for fractured and non-fractured samples.

| | $S_{or}$, % | $S_{wirr}$, % | $k_{ro}@S_{wirr}$ | $krw@S_{or}$ |
|---|---|---|---|---|
| fracture | 35.6 | 49.1 | 0.40 | 0.10 |
| non-fracture | 20.0 | 47.0 | 0.89 | 0.09 |

**Fracture in Detail:** The Amira software package was used to cut the fracture and separate it from the matrix. A range of CT numbers from 2200 to 2800 was assigned to the fracture. Because the interaction between the fluid and the matrix make it difficult to directly extract the oil and water inside the fracture, several threshold values were tested to get the optimum threshold values for water and oil in the fracture. CT numbers from 1 to 3300 were assigned to represent the oil inside the fracture and from 3301 to 5000 CT numbers were taken to represent the water. Images from 285 to 1700 that included the fracture were selected. Fracture volume was found to be 181.48 $mm^3$. The fracture was representing 0.75% of the bulk volume. Water and oil distributions and saturations were measured inside the fracture at $S_{wirr}$ and $S_{or}$ conditions.

**Residual Water Conditions:** Water and oil saturation inside the fracture are 36.4% and 63.6%, respectively. Water distribution inside the fracture at $S_{wirr}$ condition is shown in

Figure 40**.** Each color represents a strongly connected region. The red region is the most connected region representing 83% of total water in the fracture at $S_{wirr}$ condition. Figure 41 shows the oil saturation inside the fracture at $S_{wirr}$ condition. The blue region represents 70% of the total oil in the fracture. Figure 42 shows both oil and water distribution inside the fracture at $S_{wirr}$ condition, blue is the water and the red is the oil. Table 6 shows the average water and oil saturation in the fracture at $S_{wirr}$ condition.

Table 6: Water and Oil saturation inside the fracture at $S_{wirr}$ condition.

| Material | Count | Volume,$mm^3$ | Percentage |
|---|---|---|---|
| Fracture | ---------- | 181.48 | --------- |
| oil_at_swirr | 3809310 | 115.37 | 63.57 |
| water_at_swirr | 2183096 | 66.12 | 36.43 |

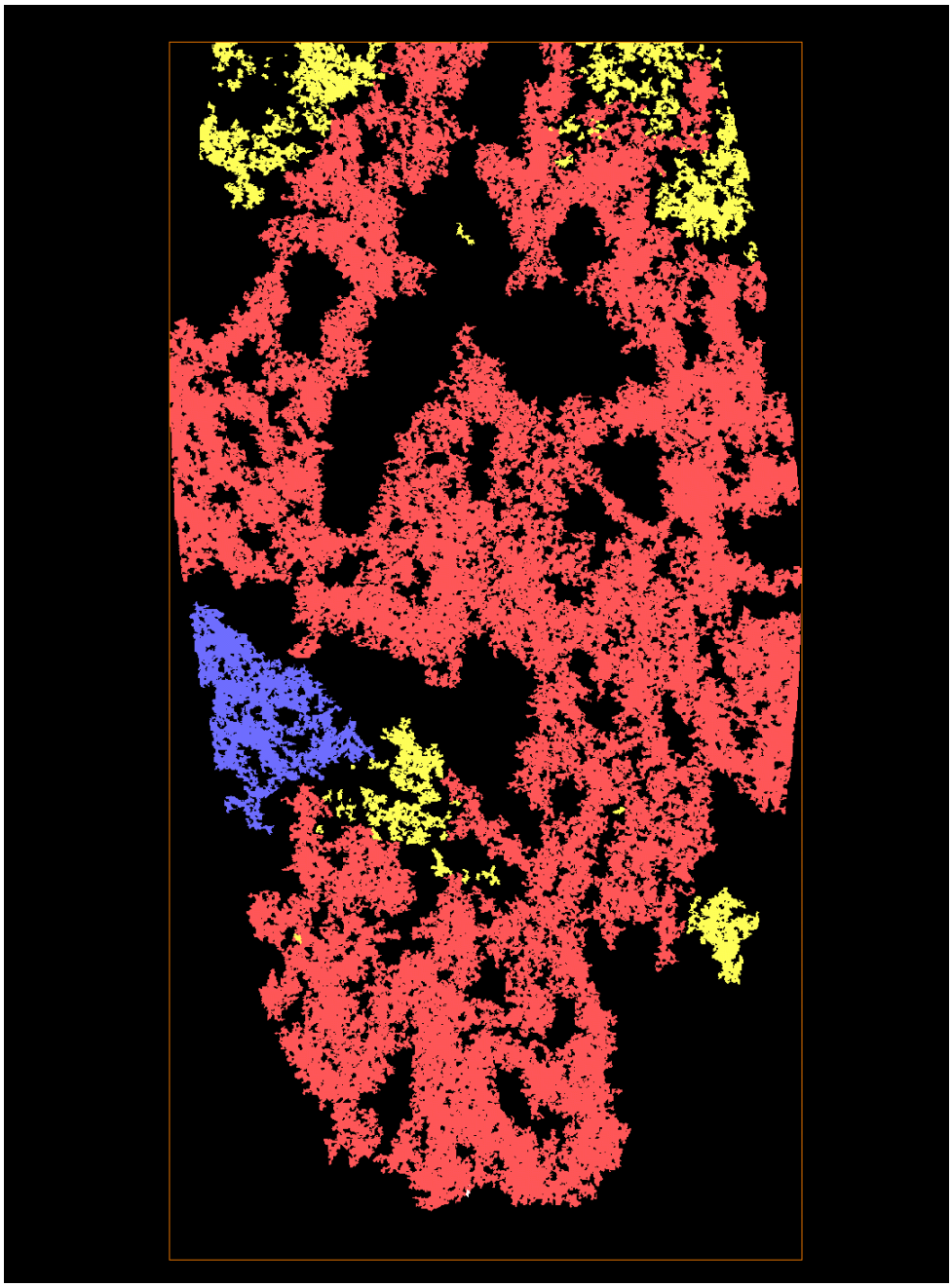

Figure 40: water saturation inside the fracture at $S_{wirr}$ condition.

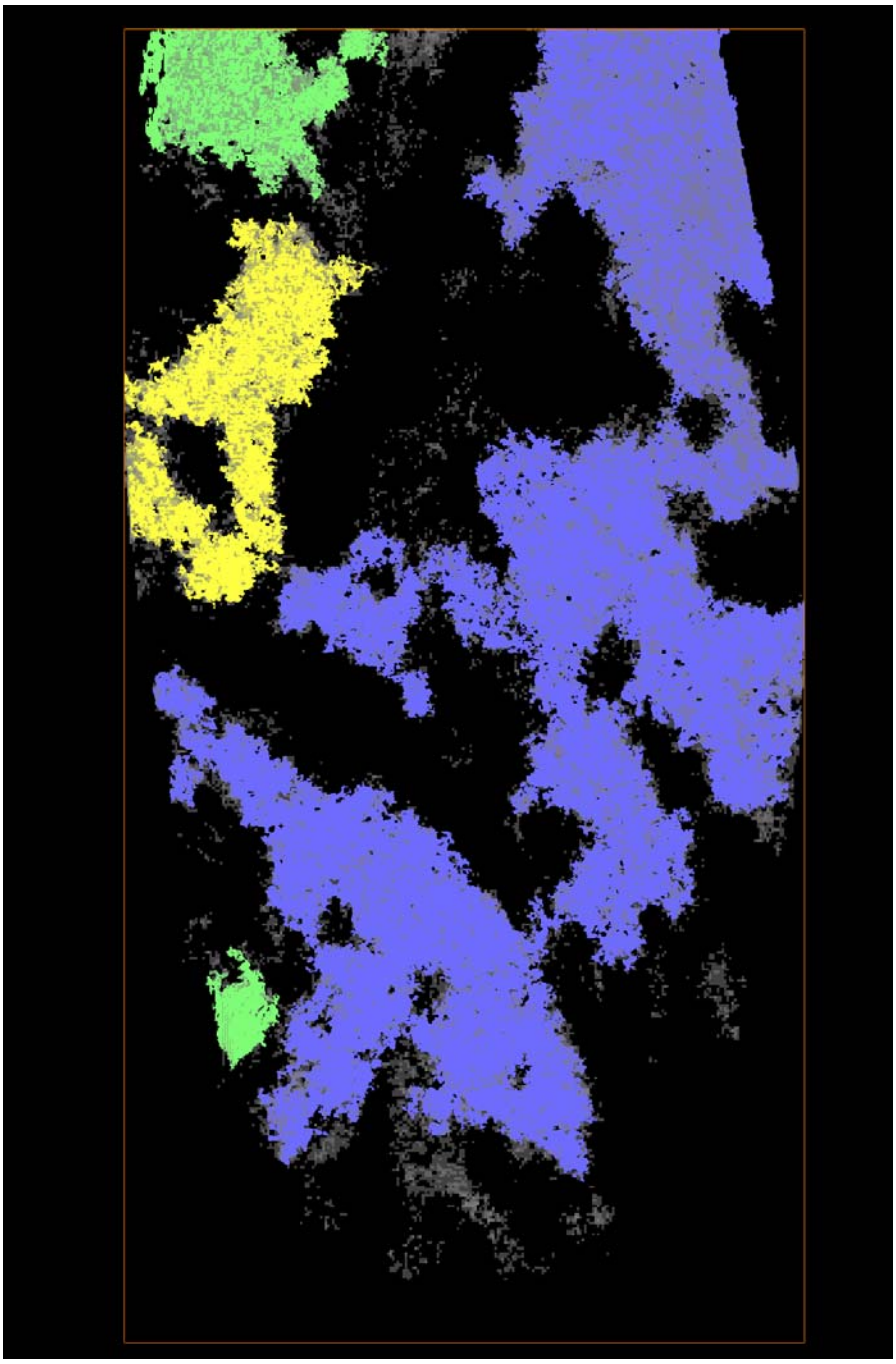

Figure 41: Oil saturation inside the fracture at $S_{wirr}$ condition. Dark gray is the fracture.

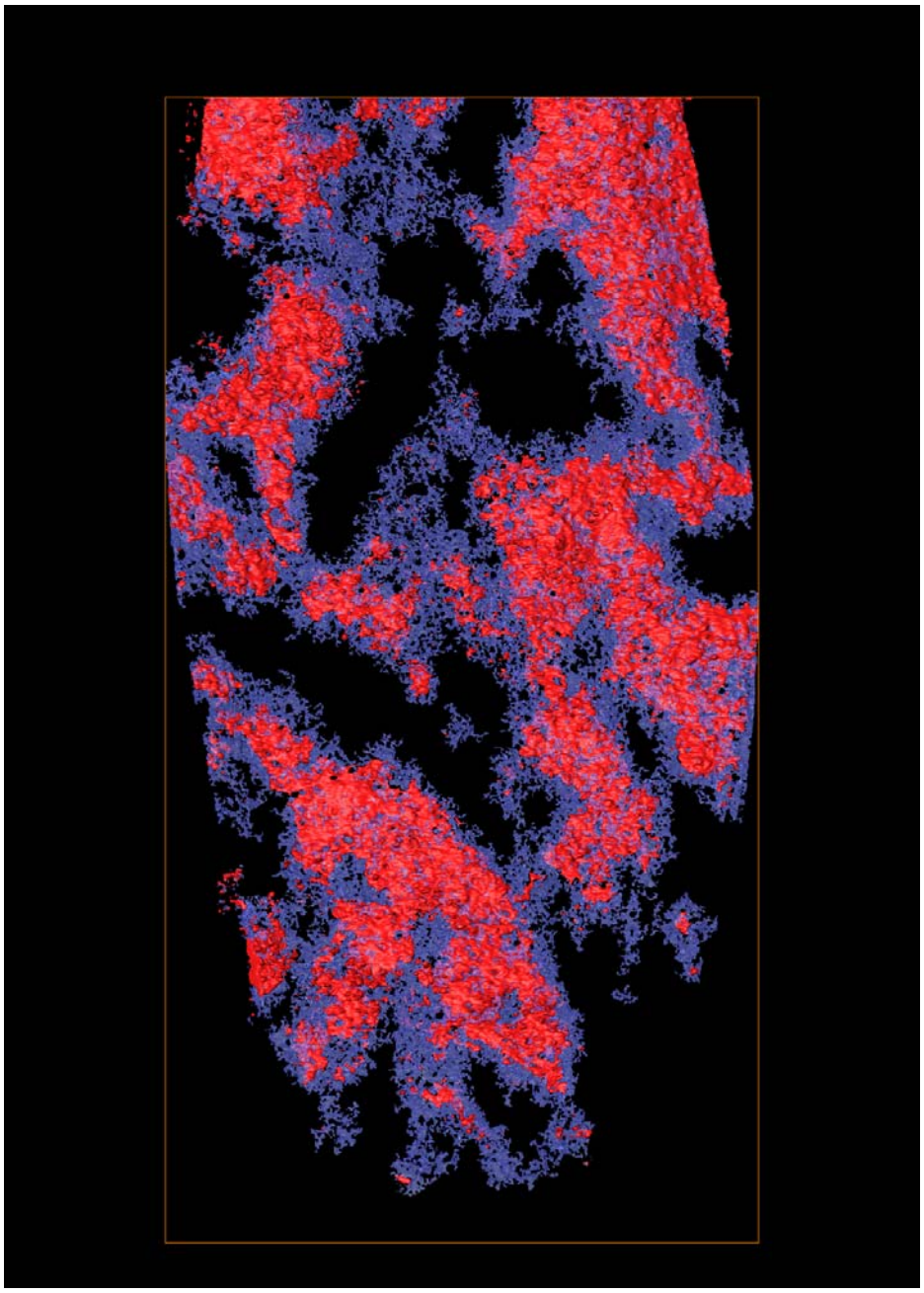

Figure 42: Both oil and water saturation at $S_{wirr}$ condition. Blue is water and red is oil.

**Residual Oil Condition**: The same analysis procedure was repeated at $S_{or}$ condition. Water and oil saturations at $S_{or}$ are 55% and 45%. Figure 43 shows the water saturation inside the fracture at $S_{or}$ condition, at this condition most of the water is connected where the connected region is 96% of the total water in the fracture. Figure 44 shows the kerosene saturation at $S_{or}$ condition. The most connected region of kerosene, blue color, represents 44% of the total oil in the fracture. Figure 45 shows water and oil distribution at $S_{or}$ condition, the blue color is the water and the red is the oil. Average water and oil saturation at $S_{or}$ condition are shown in Table **7.**

At both saturation conditions, $S_{wirr}$ and $S_{or}$, most of the water was connected. The possible reason could be that water was the wetting phase and it saturates most of the fracture's wall, while the oil concentrated in the middle of the fracture as shown in Figure 46.

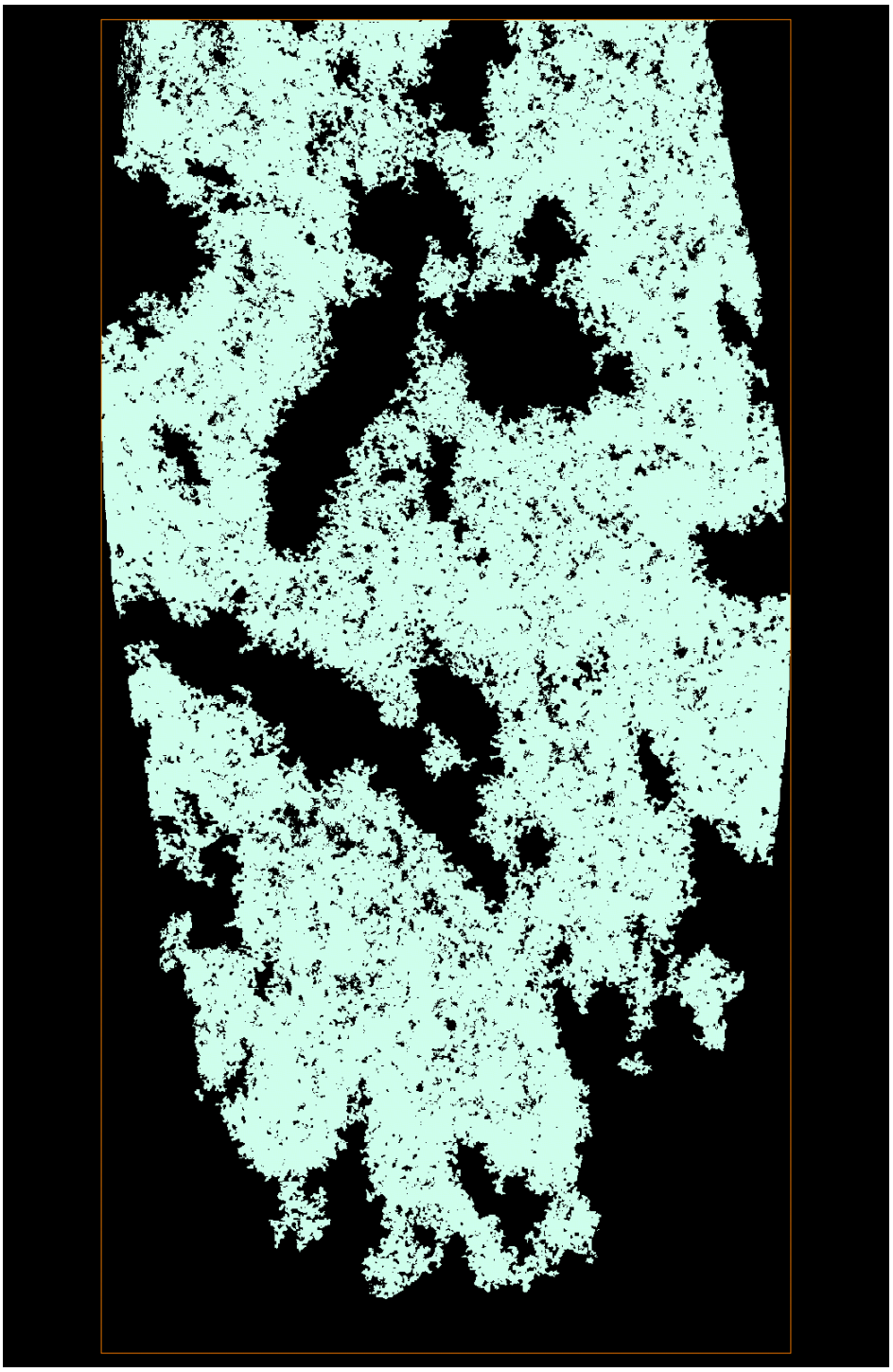

Figure 43: Water saturation inside the fracture at $S_{or}$ condition.

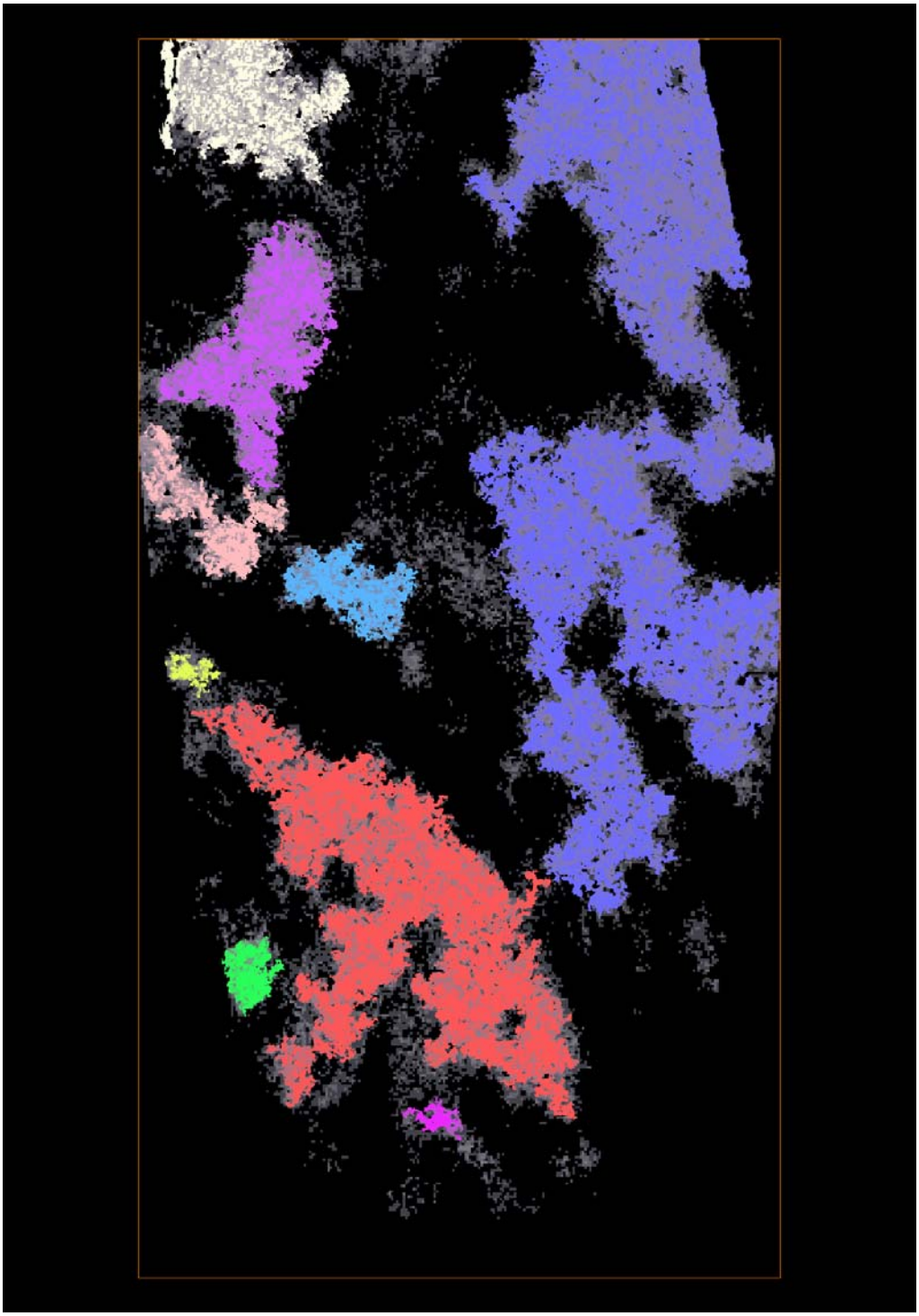



Figure 44: Oil saturation inside the fracture at $S_{or}$ condition. Dark gray is the fracture.

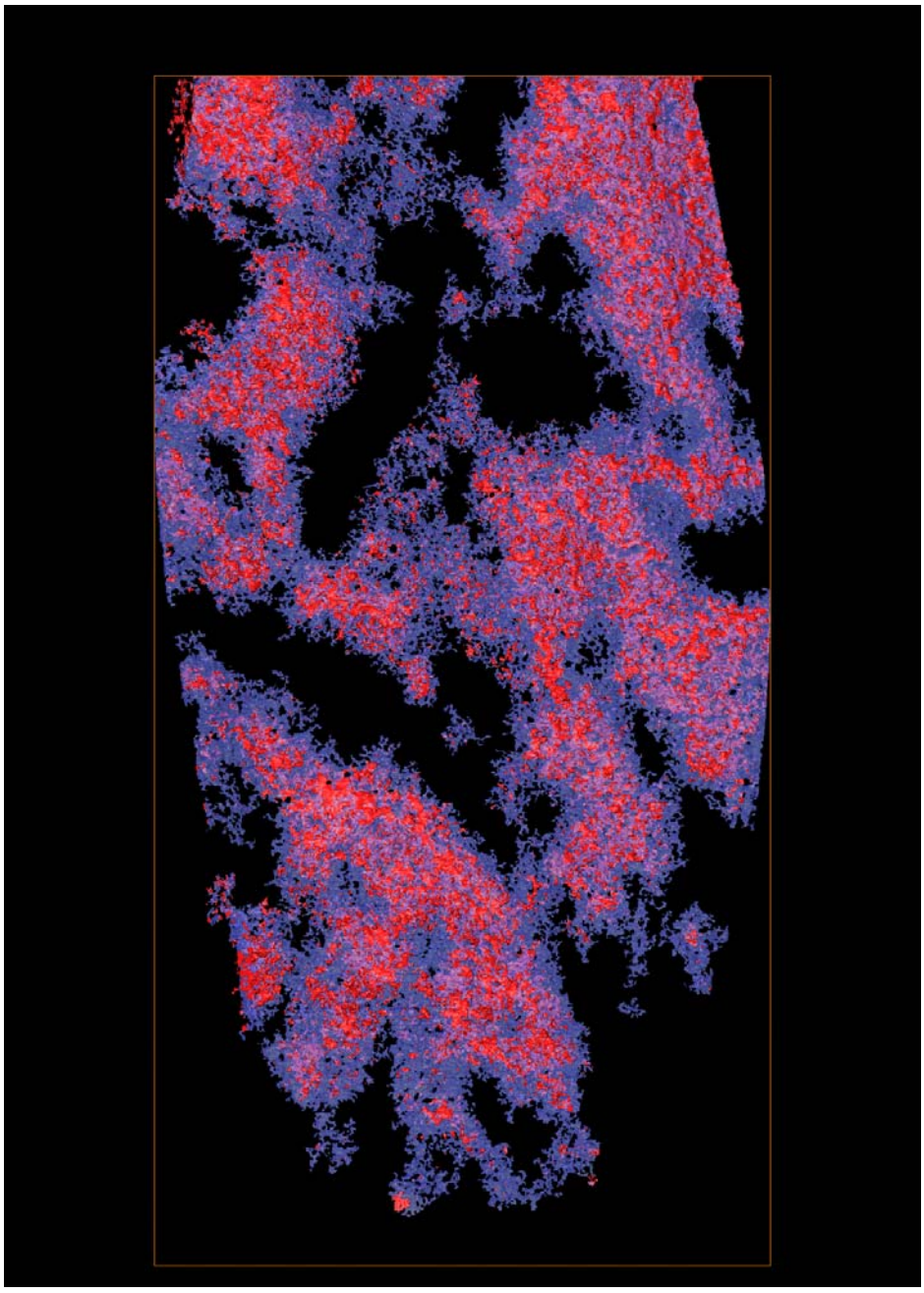

Figure 45: Both oil and water saturation at $S_{wirr}$ condition.

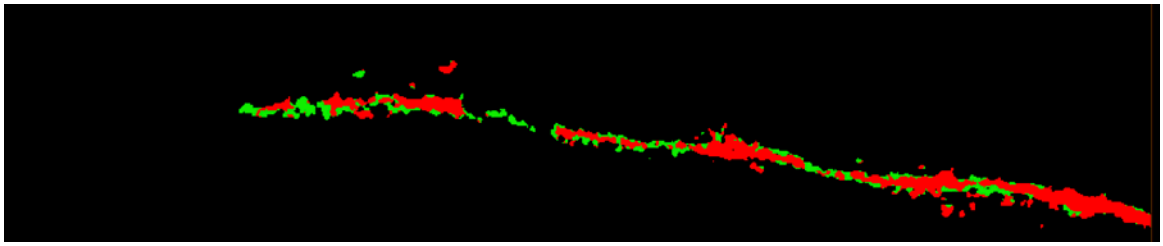

Figure 46: oil and water location inside the fracture at $S_{wirr}$ in a single CT slice.

Table 7: Water and Oil saturation at $S_{or}$ condition.

| Material | Count | Volume,$mm^3$ | Percentage |
|---|---|---|---|
| Fracture | ---------- | 181.44 | --------- |
| Oil at sor | 2698137 | 81.71 | 45.04 |
| Water at sor | 3292910 | 99.73 | 54.96 |

Table 6 and Table 7 show that about 19% of the oil was produced from the fracture after water flooding. Even though the fracture was working as a conduit to the fluid, but still the $S_{or}$ value is high. This is because most of the fracture's wall is water wet and most of the oil located at the center of the fracture in large aperture areas, so when flooding with water, the water prefers to flow mainly near the fracture wall and leaves the center of the fracture oil saturated.

**Saturation in the Matrix:** Water and kerosene saturations calculated for the fractured sample and for the fracture itself at $S_{wirr}$ and $S_{or}$ conditions were used to calculate water

and kerosene in the matrix. $S_{wirr}$ and $S_{or}$ values in the matrix are 50% and 35%, respectively. Because the volume of the fracture is very small in comparison to the pore volume of the sample, $S_{wirr}$ and $S_{or}$ in matrix are almost equal to the overall $S_{wirr}$ and sor. Table 8 shows $S_{wirr}$ and $S_{or}$ in the overall sample, fracture, and matrix

Table 8: $S_{wirr}$ and $S_{or}$ in the matrix and the fracture.

| | $S_{wirr}$, % | $S_{or}$, % |
|---|---|---|
| total sample | 49.7 | 35.6 |
| Fracture | 36.4 | 45.0 |
| Matrix | 50.3 | 35.2 |

**Observations:** The general observations of the two-phase flow experiments are:

- Water in the fracture at $S_{wirr}$ is less than at $S_{or}$.
- Oil in the fracture is more connected at $S_{wirr}$ than at $S_{or}$.
- Water is less connected in the fracture at $S_{wirr}$ than $S_{or}$, but still better connected than oil at $S_{wirr}$.
- Water appears adhered to the fracture wall at $S_{wirr}$
- The $S_{or}$ value in the fracture is 45% and is 35% in matrix.
- The $S_{wirr}$ value in fracture is 36% and in is 50% in matrix.
- $S_{wirr}$ varies along sample length. It is higher down stream. This is specific to the sample.
- Asperities and gouge formation are highly saturated with water.

## CONCLUSIONS

This exploratory study addresses the effects an artificial shear fracture created parallel to the bedding planes on absolute permeability and fluid distribution in two-phase flow experiment. Absolute permeabilities were measured before and after fracturing for shear fractures created parallel to bedding planes and perpendicular to bedding planes. Absolute permeability reduces 10% to 30% after fracturing induced parallel to bedding planes, while increases 9% to 17% after fracture induced perpendicular to bedding planes. Morphology of the fractures in both cases were compared and found that the shear fracture induced parallel to bedding planes has more asperities which distributed more than the asperities in the shear fracture induced perpendicular to bedding planes. Water and oil distributions were measured in the shear fracture induced parallel to bedding planes at Swirr and Sor saturation conditions. The value of Sor in the fracture is higher than in the matrix. Values of Swirr and Sor in a non-fractured sample were higher than the values in the fractured sample.

To better understand the effect of shear fractures on the multi-phase flow other parameters need to be evaluated, effects of confining pressure, effects of temperature, effects of wettability, effects of the fluids used in the experiments, types of porous media, displacements of the shear fracture, and core rock heterogeneities.

**REFERENCES**


Alajmi, A. F. and Grader, A. S. (2000). Analysis of Fracture-Matrix Interactions using X-Ray ct. In *Proceedings of the SPE Eastern Regional Meeting, volume 123, pages 97–104. Society of Petroleum Engineers*.

Barton, N., Bandis, S., and Bakhtar, K. (1985). Strength Deformation and Conductivity Coupling of Rock Joints. *International Journal of Rock Mechanics and Mining Sciences & Geomechanics Abstracts*, 22(3), 121–140.

Esaki, T., Du, S., Mitani, Y., Ikusada, K., and Jing, L. (1999). Development of shear flow test apparatus and determination of coupled properties for a single rock joint. *International Journal of Rock Mechanics and Mining Sciences*, vol. 36,pages 641–650.

Gentier, S., Lamontangne, E., Archambault, G., and Riss, J. (1997). Anisotropy of Flow in Fracture Undergoing Shear and its Relationship to the Direction of Shearing and Injection Pressure. *International Journal of Rock Mechanics and Mining Sciences* Vol. 34 No. (3-4), page 412.

Gentier, S., Riss, J., Archambault, G., Flamand, R., and Hopkins, D. (2000). Influence of fracture geometry on shear behaviour. *International Journal of Rock Mechanics and Mining Sciences*, Vol. 37, pages 161–174.

Karpyn, Zuleima (2005). Capillary-Driven Flow in Fractured Sandstone. PhD. Thesis, Penn State University.

Keller, A. (1998). High Resolution, Non-destructive Measurement and Characterization of Fracture Apertures. *International Journal of Rock Mechanics and Mining Sciences*, Vol. 35, No. 8, pages 1037-1050.

Makurat, A. (1985). The Effect of Shear Displacement on the Permeability of Natural Rough Joints. *In Proceedings of the 17th International Congress of the International Association of Hydrogeologists*, Vol. 39, pages 99–106.

Mohammad, Nazia (2004). Effects of Artificial Shear Fracture on Two-Phase Flow in Berea Sandstone. Ms. Thesis, Penn State University,

Montemagno, C. D., Pyrak-Notle, L. J. (1999). Fracture Network Versus Single Fractures: Measurement of Fracture Geometry with X-ray Tomography. *Phys. Chem. Earth (A)*, Vol. 24, No. 7, pages 575-579.

Olsson, W. A., Brown, S. R., (1993). Hydromechanical Response of A fracture Undergoing Compression and Shear. *International Journal of Rock Mechanics and Mining Sciences, Geomech. Apstr.* 30, 845-851.

Teufel, L. W. (1987). Permeability Changes During Shear Deformation of Fractured Rock. *In Proceedings of the 28th U.S. Symposium on Rock Mechanics*, volume 129, pages 473–480.

## LIST OF ACRONYMS AND ABBREVIATIONS